minerals

MDPI

*Article*

# Apatite U-Pb Dating and Composition Constraints for Magmatic–Hydrothermal Evolution in the Giant Renli Nb-Ta Deposit, South China

**Yongsheng Cheng [1,2], Zhuobin Xu [1,2,*], Hongfei Di [1,2,*], Zewen Zhang [1,2], Chunwang Mao [1,2], Huajie Tan [1,2], Jianzhong Huang [3], Fangchun Zhou [4], Liping Zhang [4], Jianfeng Chen [3] and Chunhua Wen [3]**

[1] Key Laboratory of Metallogenic Prediction of Nonferrous Metals and Geological Environment Monitoring (Central South University), Ministry of Education, Central South University, Changsha 410083, China; cys968@163.com (Y.C.); zzw205001002@163.com (Z.Z.); mchunwang@126.com (C.M.); huajietan23@163.com (H.T.)
[2] School of Geosciences and Info-Physics, Central South University, Changsha 410083, China
[3] Hunan Institute of Geological Survey, Changsha 410116, China; ddyhjz@126.com (J.H.); chenjianfeng021041@163.com (J.C.); herowch2004@163.com (C.W.)
[4] Hunan Institute of Geological Disaster Investigation and Monitoring, Changsha 410100, China; zhoufangchun311@163.com (F.Z.); zhang907690548@163.com (L.Z.)
* Correspondence: 8205180302@csu.edu.cn (Z.X.); 8211180903@csu.edu.cn (H.D.)

**Abstract:** Apatite is a nearly ubiquitous accessory phase in igneous rocks that crystallizes during the entire magma evolution process and has great implications for geochronology and petrogenesis. Previous studies suggested that Nb-Ta mineralization in the giant Renli deposit was genetically related to Late Jurassic two-mica monzogranite or Early Cretaceous muscovite monzogranite. Moreover, the magmatic–hydrothermal evolution of these two stages is poorly understood. In our study, we confirm that the muscovite monzogranite, biotite monzogranite, and two-mica monzogranite are all spatially associated with Nb-Ta pegmatites. We present new apatite U-Pb ages to constrain the timing of Nb-Ta mineralization and related magmatism. The results show that apatite from the two-mica pegmatite yield a lower intercept age of 130 ± 2 Ma (2σ), and apatite grains from two two-mica pegmatite samples yield a lower intercept age of 135 ± 8 Ma (2σ) and 134 ± 3 Ma (2σ), respectively. Apatite and whole-rock geochemistry suggest the oxidation degree of the Nb-Ta mineralization increases from north (RL-6) to south (RL-16) in the giant Renli deposit. This study demonstrates that a combination of apatite composition and U-Pb ages can be used to constrain the magmatic–hydrothermal evolution of granite and pegmatite-type Nb-Ta deposits.

**Keywords:** apatite U-Pb age; trace elements; magmatic–hydrothermal evolution; Renli pegmatite Nb-Ta deposit; South China

**Citation:** Cheng, Y.; Xu, Z.; Di, H.; Zhang, Z.; Mao, C.; Tan, H.; Huang, J.; Zhou, F.; Zhang, L.; Chen, J.; et al. Apatite U-Pb Dating and Composition Constraints for Magmatic–Hydrothermal Evolution in the Giant Renli Nb-Ta Deposit, South China. *Minerals* **2022**, *12*, 344. https://doi.org/10.3390/min12030344

Academic Editor: Kunfeng Qiu

Received: 28 December 2021
Accepted: 10 March 2022
Published: 11 March 2022



## 1. Introduction

The Nb-Ta deposits represent an important source of critical metals and minerals, and therefore they play an important role in the national defense industry, the aerospace industry, the nuclear industry, super-hard materials industry, and other industries [1,2]. Apatite is a ubiquitous accessory mineral in granite and pegmatite-type Nb-Ta deposits and can carry many trace elements during the entire magmatic–hydrothermal evolution process [3,4]. The occurrence of trace elements (e.g., U, Th, Sr, and REE) in apatite is controlled by melt/phosphate mineral equilibria, the composition of the host rock, and physico-chemical conditions [4–7]. Therefore, apatite can be used to decipher petrogenesis and constrain magmatic processes. The crystal structure of apatite and the radioactive decay of U and Th make it an ideal mineral for thermochronology and yields crystallization ages of rapidly cooled plutonic rocks using the U–Pb system [8–11]. LA-ICP-MS (Laser

ablation-inductively coupled plasma-mass) apatite U-Pb dating can exhibit weighted mean age uncertainties as low as 1–2% [12]. Therefore, apatite U-Pb geochronology can provide valuable information on the timing of thermal events.

The Renli ore field is an important resource area of rare elements in the Mufushan region, South China [13]. The relationship between Nb-Ta mineralization and granite (two-mica monzogranite or muscovite monzogranite) in the giant Renli Nb-Ta deposit has been reported [14,15]. However, it continues to be a controversial topic. Moreover, the magmatic–hydrothermal evolution of the mineralization in this giant Renli Nb-Ta deposit is poorly understood. Three interspersed pegmatite veinlets with various compositions in the granite of the Renli Nb-Ta deposit were identified. In this study, we investigate the textures and composition of apatites of granites from the giant Renli Nb-Ta deposit to constrain the Renli granite ages and the magmatic–hydrothermal evolution.

## 2. Geological Setting

### *2.1. Regional Geological Setting*

The giant Renli Nb-Ta deposit is located at the southwestern margin of the Mufushan composite granite, which belongs to the central Jiangnan Orogen in South China (Figure 1a). It is considered a continent–continent collisional belt between the Yangtze Block and Cathaysia Block [16–19]. The exposed strata in the area are the Qingbaikou, the Sinian, the Cambrian, the Cretaceous, and the Quaternary system [20]. The Lengjiaxi group of the Qingbaikou system is a set of shallow metamorphic clastic rock series, which are exposed in the southwest of the Mufushan complex and belong to the metamorphic basement of the Yangtze block (Figure 1b). The Jiangnan Orogen belt is characterized by a series of NE-, EW-, and WNW-trending faults, including the NE-trending Taolin fault, the Jiujitou–Sugujian deep fault, the Zhangguchong–Fenglin compressive torsional fault, the Tianbaoshan–Shijiang compressive torsional fault, the NW-trending Changtang–Yuetian–Nanjiang deep fault, and the Baowan–Yaojiadong compressive torsional fault [21,22]. Regional-scale NE-trending faults control the distribution of Late Mesozoic granites along them, which are the most common type of pluton.

Four major magmatic events have been documented in South China; in particular, magmatic rocks formed during the Early Cretaceous (130–129 Ma) exhibit similar geological characteristics [14,19,23–26]. The Mufushan composite granite in the middle of the Jiangnan orogenic belt was formed during the Yanshanian stage and is closely related to rare-metals mineralization (Figure 1). It consists of complex intrusions, such as monzogranite, biotite granodiorite, biotite monzogranite, and two-mica monzogranite, which are Neoproterozoic-Late Mesozoic rocks [27]. Abundant rare-metal deposits have been discovered to be associated with the Mufushan composite granite, including the Renli Nb-Ta, Chuanziyuan Li-Nb-Ta, and Baishawo Be-Nb-Ta deposits [20,28–30].

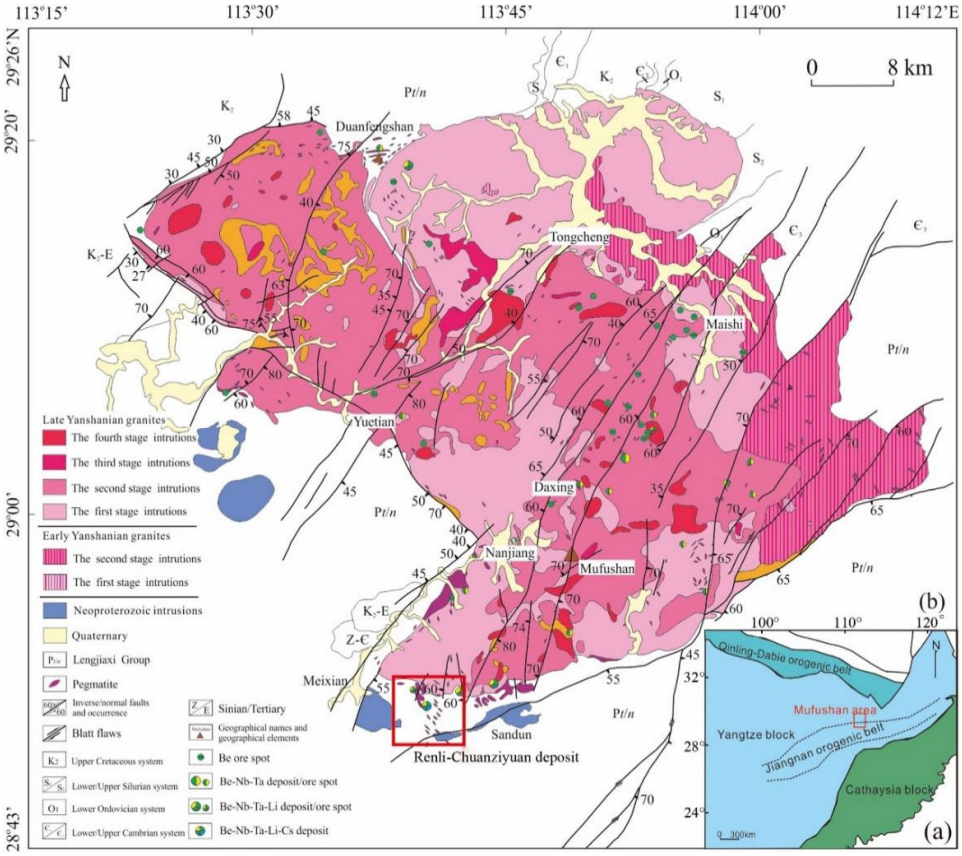


**Figure 1.** The location of the study area (**a**) and geological map (**b**) of the Mufushan area (modified after [19,27]).

### *2.2. Geological Setting of the Renli Nb-Ta Deposit*

The Renli Nb-Ta deposit is hosted within the pegmatite that is one part of the Mufushan composite granite [31] (Figure 2). It is a high-grade Nb-Ta rare-metal deposit (14,057 t of $Nb_2O_5$, average grade at 0.047 wt.%; 10,791 t of $Ta_2O_5$, average grade at 0.036 wt.%; [15,32]). The strata exposed in the mining area, from young to old, are the Quaternary sequences and the Neoproterozoic Pingyuan formation of the Lengjiaxi group, respectively. The Lengjiaxi group includes mainly banded slate, sericite schist, and garnet-bearing mica schist [32]. The main structures in the mining area are the NE-trending Tianbaoshan-Shijiang fault, the NNE-trending Jiangjiafang–Nanjiang fault, the Tuozhuangqiao–Jiangbei fault, and the SN-trending Huangboshan fault (Figure 2). The NE-trending Tianbaoshan–Shijiang fault and the Huangboshan fault control the Renli–Chuanziyuan deposit (Figure 2 [14]).

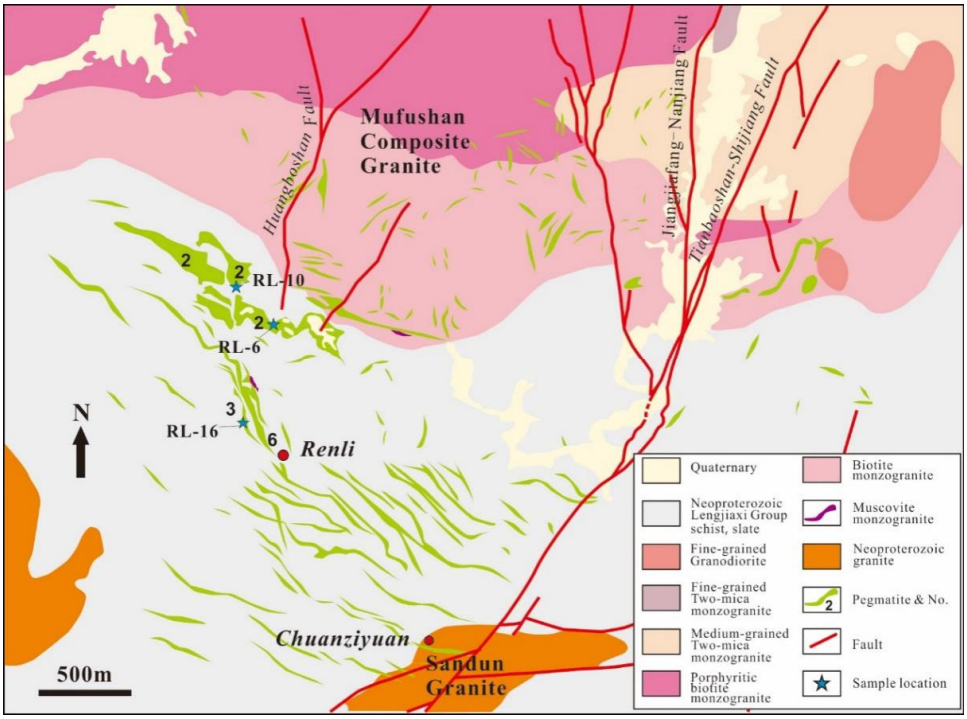


**Figure 2.** Geological map of the Renli Nb-Ta deposit (modified after [14]). RL is the abbreviation for Renli.

The magmatic activity in the area was intense, and the outcropping magmatic rocks contain the Neoproterozoic and Yanshanian granitic rocks. The magmatic rocks can be divided into three types: (1) The large-size Yanshanian Mufushan granitoid found in the north, and composed of the Late Jurassic coarse- to medium-grained biotite monzogranite and Early Cretaceous fine-to-medium-grained muscovite monzogranite. Biotite monzogranites appear in a large area of the batholith and are divided into marginal and transitional phases. The muscovite monzogranite is in a rocky area and has a clear boundary with the first stage intrusion, generally sericitization and albitization [30]. They are closely related to rare-metal mineralization [19]. (2) The Neoproterozoic coarse-to-medium-grained biotite monzonitic granite is outcropped in the west (including the Meixian and Sandun plutons). (3) The Neoproterozoic medium-to-fine-grained two-mica plagioclase granite is developed in the southeast (Figure 2). The biotite monzogranite and two-mica monzogranite are closely spatially related to pegmatites (Figure 3a,b). The biotite monzogranites show a porphyritic structure in hand specimens and consist of quartz (35–45 vol.%); K-feldspar (15–20 vol.%); plagioclase (15–20 vol.%); biotite (8–10 vol.%); and minor amounts of zircon, chlorite, apatite, and pyrite (Figure 3a). The two-mica monzogranites consist of quartz (30–35 vol.%), K-feldspar (25–30 vol.%), plagioclase (20–25 vol.%), muscovite (5–10 vol.%), and biotite (5–10 vol.%) (Figures 3b and 4c).

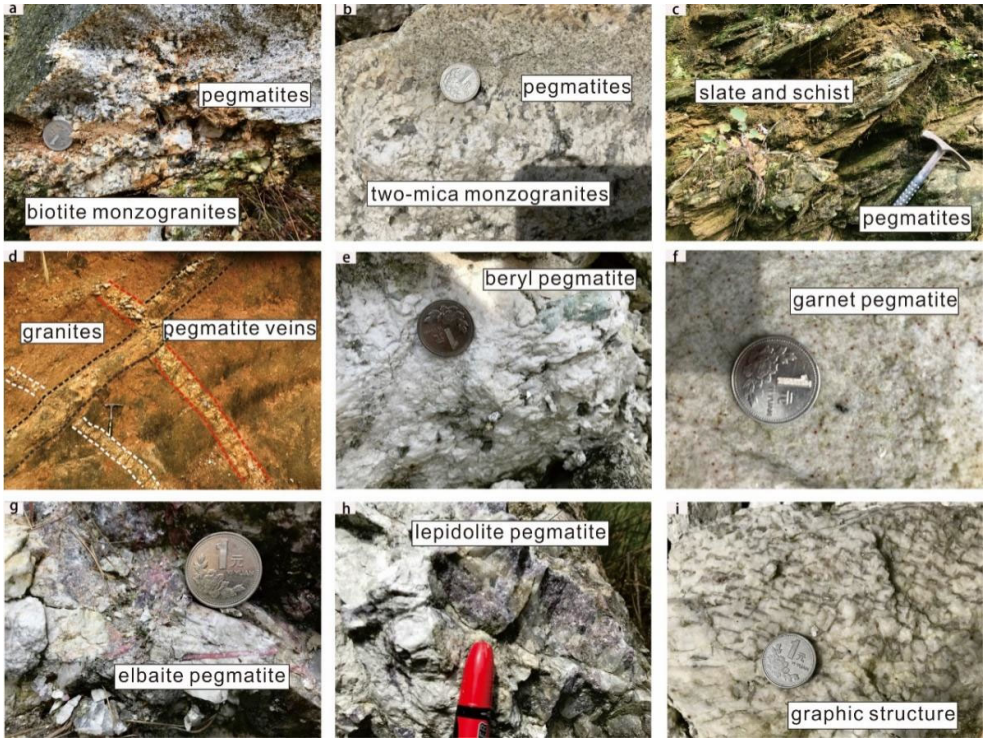


**Figure 3.** Field photographs showing features of granites and pegmatites in the Renli Nb-Ta deposit: (**a**) biotite monzogranites with porphyritic structure; (**b**) weakly gneissic two-mica monzogranites; (**c**) pegmatite contact with schist of the Lengjiaxi group; (**d**) three pegmatite veinlets with various compositions interspersed in the granite; (**e**–**h**) beryl pegmatite, garnet pegmatite, elbaite pegmatite, and lepidolite pegmatite in the Renli deposit; (**i**) pegmatite with graphic structure.

A total of 926 pegmatite veinlets have been discovered in the Renli Nb-Ta deposit, and 712 and 214 veinlets crosscut into the granite intrusions and the Lengjiaxi group schist, respectively [15,19]. Nb-Ta pegmatite veinlets occur mostly in the Lengjiaxi group adjacent to the contact zone and cut the slate and schist of the Lengjiaxi group and the Mufushan composite granite (Figures 3c,d and 4f). The occurrences of Nb-Ta-rich pegmatite dikes are controlled by the bedded structure of sedimentary rocks and Mesozoic granite [14]. From the northeast to the southwest of the Renli Nb-Ta deposit, the volume of the veins decreases, and the mineralization type become complex (Be → Be + Nb + Ta → Be + Nb + Ta + Li) [13,27].

## 3. Samples and Methods

Samples RL-6 and RL-10 were collected from the No. 2 pegmatite, and RL-16 was collected from the No. 3 pegmatite in the Renli deposit (Figure 2). Other samples were all collected near the central part of deposit. All samples were analyzed for whole-rock geochemistry, LA-ICP MS apatite U-Pb dating, and apatite geochemistry. After crushing the rock samples, apatite grains were separated by standard heavy liquid and magnetic separation techniques, and then handpicked under a binocular microscope, mounted in an epoxy resin, and polished. Before apatite U-Pb dating and analysis of major and trace elements, samples were polished into thin sections (50 μm thickness) for microscopic observation; backscattered electron (BSE) and cathodoluminescence (CL) imaging of the apatite grains was undertaken at the Guangzhou Tuoyan Analytical Technology Co., Ltd., Guangzhou, China.

### *3.1. Whole-Rock Geochemistry Analyses*

The whole-rock geochemistry was analyzed at the Guangzhou Tuoyan Analytical Technology Co., Ltd., Guangzhou, China. All the samples from pegmatites were ground to a c. 200 mesh size in an agate mortar. Major element content was determined using an X-ray fluorescence (XRF) spectrometer (XRF-1500) and fused glass discs. Ferric and ferrous iron measurements were performed via wet chemical analyses: acid decomposition and titration with potassium dichromate [15]. The analytical precisions were ≤0.01 wt.% for major elements analyses. An Agilent 7500a system was used to determined trace element concentrations by inductively coupled plasma-mass spectrometry (ICP-MS). The detailed experimental procedure can be found in Xiong et al. [14]. The analytical precisions were ≤5% for the trace element and rare-earth element (REE) analyses.

### *3.2. Major and Trace Element Analyses of Apatite*

The chemical compositions of apatite were analyzed at the Guangzhou Tuoyan Analytical Technology Co., Ltd., Guangzhou, China, with a JEOL JXA-8100 Electron Micro Probe Analyzer (EMPA) equipped with four wavelength-dispersive spectrometers (WDS). Before the analysis, the samples were first coated with a thin conductive carbon film. We used an accelerating voltage of 15 kV, a beam current of 20 nA, and a 5 μm spot size. The peak counting time was 10 s for Ca and P, and 20 s for Na, Mg, Si, Fe, Mn, Sr, F, and Cl. The following standards were used: olivine (Fe), rhodonite (Mn), diopside (Mg), celestite (Sr), phlogopite (F), tugtupite (Cl), apatite (Ca, P), and jadeite (Na, Si). Precision was generally better than 5% for element content >0.5 wt.% and better than 1% for element content >10 wt.% [4]. LA-ICP-MS analysis of trace elements in apatite was also carried out at the Guangzhou Tuoyan Analytical Technology Co., Ltd., Guangzhou, China, using an Agilent 7500a ICP-MS and Geolas 193 nm laser. The SRM 610 glass standards and the two MAD glasses were repeatedly analyzed after every eight apatite samples. A 33 μm spot size, a 10 Hz repetition rate, and a corresponding energy density of ~3 J/cm$^2$ were used. The Ca measured by EMPA was used as the internal standard to correct the low and high content of trace elements in apatite.

### *3.3. LA-ICP-MS Apatite U-Pb Dating*

Apatite U-Pb dating was conducted at the Guangzhou Tuoyan Analytical Technology Co., Ltd., Guangzhou, China, by a laser ablation-inductively coupled plasma-mass spectrometry (LA-ICP-MS) instrument using a Resolution 193 nm laser-ablation system coupled to a Thermo iCAP RQ ICP-MS instrument. The Madagascar apatite (MAD) U-Pb ages of 485.0 ± 1.7 Ma were used as the external isotopic calibration reference material [33]. The $^{206}Pb/^{238}U$ ratio is 0.0762 and $^{207}Pb/^{235}U$ ratio is 0.6013 for the MAD measurements. Each set of eight or nine sample analyses was followed by one measurement of SRM 610 and three measurements of MAD. Before analysis, single apatite grains were mounted in epoxy and polished. Then, they were ablated in a continuous He stream. Before entering a Thermo iCAP RQ ICP-MS, the He stream was mixed with $N_2$ and Ar downstream. Samples and standards were ablated with a 33 μm laser spot, a repetition rate of 8 Hz, and a 4 J/cm$^2$ energy density. Furthermore, the $^{206}Pb/^{238}U$ ages are reported at an uncertainty level of 2$\sigma$ [19]. The detailed data reduction process can be found in Chew et al. and Petrus et al. [34,35].

## 4. Results

### *4.1. Apatite Texture*

The micrograph and backscattered electron (BSE) images of apatite from the Renli Nb-Ta deposit are shown in Figures 4 and 5. The pegmatite consists of quartz, K-feldspar, albite, muscovite, beryl, garnet, tourmaline, and lepidolite and has a figurative structure (Figures 3e–i and 4a,b,d,e). Apatites from pegmatite of the Renli Nb-Ta deposit is subhedral to anhedral and up to 50–100 μm in length (Figure 4g–i). The apatites also show

homogeneous texture without obvious fractures and inclusions in BSE images (Figures 4g–i, 5). They usually occur as a single mineral or as an inclusion in other minerals.

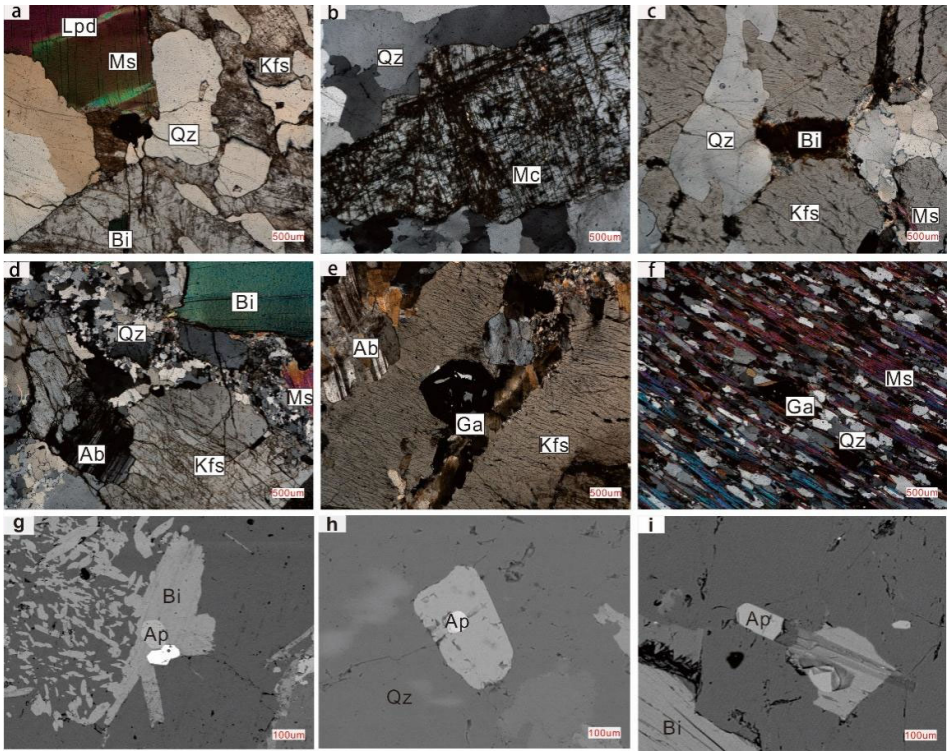


**Figure 4.** Photomicrographs showing the features of granite and pegmatite from the Renli Nb-Ta deposit: (**a**) lithium mica pegmatite; (**b**) microcline pegmatite; (**c**) two-mica monzogranites; (**d**) beryl pegmatite; (**e**) garnet pegmatite; (**f**) garnet-bearing schist; (**g**–**i**) BSE images of apatite in pegmatite. Ab = albite; Bi = biotite; Grt = garnet; Kfs = K-feldspar; Lpd = lepidolite; Mc = microcline; Ms = muscovite; Qz = quartz.

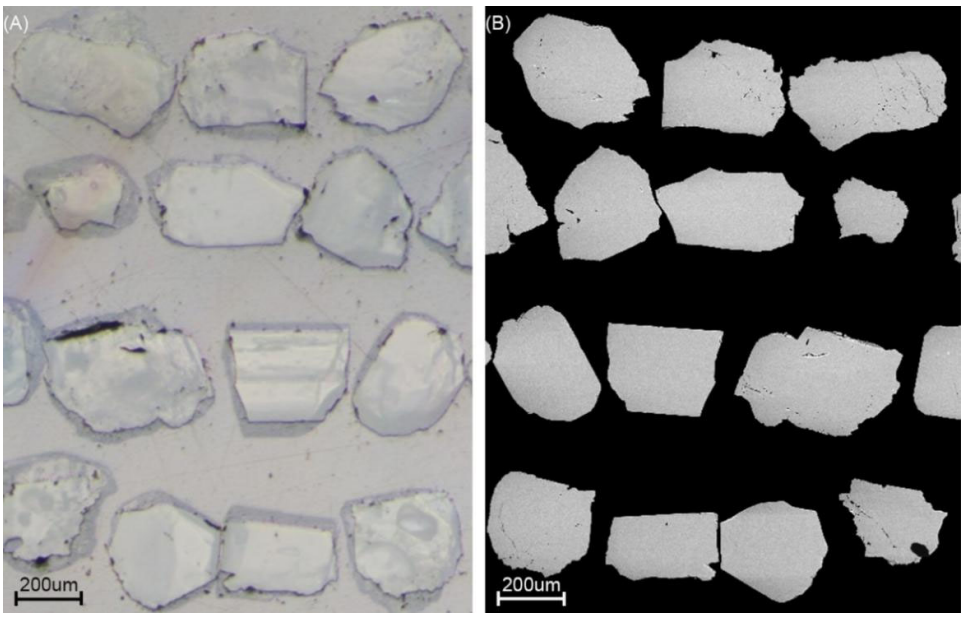


**Figure 5.** The (**A**) micrograph and (**B**) backscattered electron (BSE) images of apatite from RL-6, RL-10, and RL-16.

### *4.2. Whole-Rock Geochemistry*

Major and trace elements composition of pegmatite from the Renli Nb-Ta deposit are listed in Tables 1 and 2. The levels of loss on ignition (LOI) of most samples are less than 1 wt.%, indicating that post-magmatic alteration or weathering is not obvious. The pegmatite has a relatively wide range of chemical compositions in the Renli Nb-Ta deposit. $Al_2O_3$ and $K_2O$ content broadly decrease with increasing $SiO_2$; the content of $Na_2O$ increases with increasing $SiO_2$, whereas Cao, MgO, and $Fe_2O_3$ content do not show an obvious correlation with $SiO_2$ (Figure 6).

**Table 1.** Major elements composition of the pegmatite from Renli Nb-Ta deposit (wt.%).

| Sample | $SiO_2$ | $TiO_2$ | $Al_2O_3$ | $Fe_2O_3$ | MnO | MgO | CaO | $Na_2O$ | $K_2O$ | $P_2O_5$ | BaO | LOI |
|---|---|---|---|---|---|---|---|---|---|---|---|---|
| RL-1 | 72.26 | 0.01 | 14.74 | 0.38 | 0.01 | 0.02 | 0.08 | 2.25 | 9.60 | 0.04 | 0.01 | 0.19 |
| RL-2 | 76.28 | 0.04 | 14.26 | 0.93 | 0.03 | 0.10 | 0.71 | 5.29 | 1.67 | 0.08 | <0.01 | 0.84 |
| RL-5 | 73.80 | 0.01 | 14.20 | 0.56 | 0.04 | 0.03 | 0.19 | 2.89 | 6.95 | 0.04 | 0.01 | 0.55 |
| RL-6 | 76.30 | 0.05 | 14.48 | 0.82 | 0.02 | 0.12 | 1.11 | 4.92 | 1.49 | 0.02 | 0.01 | 0.76 |
| RL-7 | 74.68 | 0.04 | 14.72 | 0.64 | 0.02 | 0.09 | 0.78 | 3.64 | 4.41 | 0.02 | 0.01 | 0.81 |
| RL-8 | 71.86 | <0.01 | 14.94 | 0.32 | 0.01 | 0.01 | 0.06 | 1.62 | 10.35 | 0.02 | 0.02 | 0.38 |
| RL-10 | 73.93 | 0.03 | 15.01 | 0.71 | 0.03 | 0.07 | 0.19 | 3.78 | 4.73 | 0.01 | 0.01 | 0.83 |
| RL-11 | 74.61 | 0.02 | 14.53 | 0.96 | 0.03 | 0.09 | 0.11 | 2.51 | 5.99 | 0.02 | 0.01 | 1.00 |
| RL-16 | 66.04 | <0.01 | 18.66 | 0.11 | 0.01 | <0.01 | 0.03 | 2.29 | 12.25 | 0.05 | <0.01 | 0.50 |
| RL-19 | 64.69 | <0.01 | 18.88 | 0.07 | 0.01 | 0.01 | 0.02 | 1.94 | 13.35 | 0.04 | 0.01 | 0.27 |
| RL-20 | 72.36 | 0.01 | 17.03 | 0.45 | 0.03 | 0.04 | 0.76 | 7.98 | 0.84 | 0.03 | <0.01 | 0.65 |
| RL-21 | 68.04 | 0.69 | 15.62 | 5.75 | 0.13 | 1.62 | 0.51 | 1.16 | 3.39 | 0.13 | 0.06 | 2.74 |
| RL-22 | 70.47 | 0.71 | 14.27 | 5.81 | 0.11 | 1.40 | 0.38 | 0.86 | 3.65 | 0.10 | 0.07 | 2.16 |
| RL-23 | 74.50 | 0.03 | 14.38 | 0.90 | 0.04 | 0.06 | 0.26 | 3.04 | 5.67 | 0.02 | <0.01 | 0.86 |
| RL-24 | 65.13 | <0.01 | 18.92 | 0.20 | 0.01 | <0.01 | 0.04 | 2.46 | 12.90 | 0.05 | <0.01 | 0.33 |

RL: abbreviation of "Renli deposit"; <0.01 indicate that the value is under MDL.

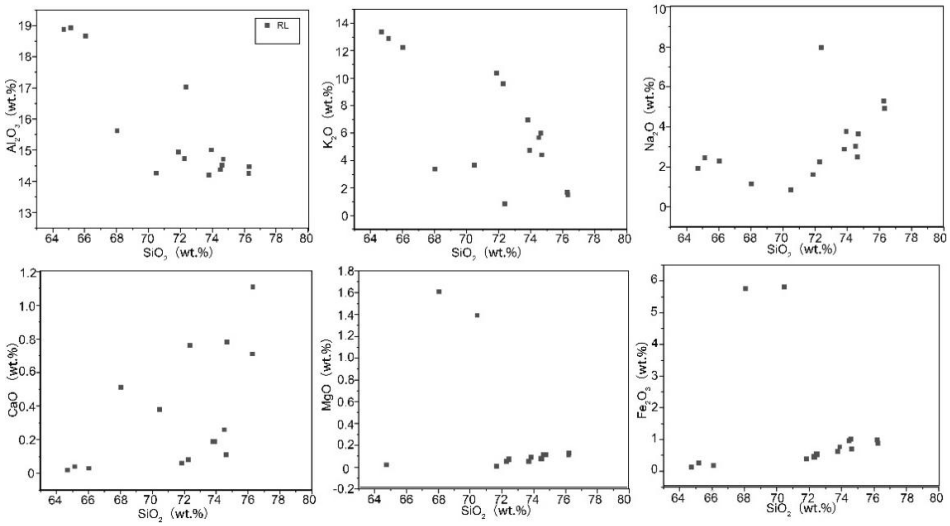


**Figure 6.** Variation diagram of $Al_2O_3$, $K_2O$, $Na_2O$, Cao, MgO, and $Fe_2O_3$ content versus the $SiO_2$ content.

The chondrite- and primitive-mantle-normalized REE [36] and trace element patterns for the studied pegmatite are shown in Figure 7. The average total rare earth element (ΣREE) contents of pegmatite in Renli is 56.63 ppm. The $(La/Yb)_N$ ratios range from 1.37 to 24.72, and the Eu/Eu * ratios range from 0.11 to 2.49 in the Renli deposit. The pegmatite from Renli has high LREE/HREE (3.03–43.63). The pegmatites from Renli are enriched in light rare earth elements (LREEs) and depleted in medium (MREEs) and heavy rare earth elements (HREEs) slightly.

**Table 2.** Trace elements composition for the pegmatite from Renli Nb-Ta deposit (ppm).

| Sample | RL-1 | RL-2 | RL-5 | RL-6 | RL-7 | RL-8 | RL-10 | RL-11 | RL-16 | RL-19 | RL-20 | RL-21 | RL-22 | RL-23 | RL-24 |
|---|---|---|---|---|---|---|---|---|---|---|---|---|---|---|---|
| Li | 21.1 | 78.7 | 41.8 | 111 | 59.3 | 24.1 | 141 | 163 | 115 | 222 | 188 | 194 | 258 | 176 | 48.2 |
| Be | 1.92 | 10.4 | 10.7 | 6.74 | 8.41 | 1.07 | 7.27 | 6.92 | 3.76 | 2.45 | 12.3 | 3.20 | 2.26 | 5.56 | 2.40 |
| Sc | 0.10 | 0.80 | 0.40 | 2.00 | 1.70 | 0.20 | 1.40 | 0.50 | 0.10 | <0.1 | 0.20 | 14.6 | 13.2 | 0.80 | <0.1 |
| Cr | 5.00 | 7.00 | 14.0 | 7.00 | 4.00 | 5.00 | 8.00 | 15.0 | 3.00 | 3.00 | 7.00 | 58.0 | 56.0 | 5.00 | 2.00 |
| Co | 0.10 | 0.20 | 0.60 | 0.30 | 0.30 | 0.20 | 0.20 | 0.20 | <0.1 | <0.1 | 0.10 | 12.9 | 13.6 | 0.20 | 0.10 |
| Ni | 0.30 | 0.30 | 1.30 | 0.30 | 0.40 | 0.40 | 0.30 | 0.70 | <0.2 | <0.2 | 0.50 | 27.5 | 25.2 | 0.30 | <0.2 |
| Cu | 1.00 | 2.30 | 2.70 | 0.80 | 1.20 | 3.20 | 4.40 | 1.30 | 0.80 | 0.30 | 6.80 | 1.10 | 45.6 | 11.5 | 2.10 |
| Zn | 9.00 | 30.0 | 12.0 | 14.0 | 12.0 | 3.00 | 26.0 | 56.0 | 4.00 | <2 | 24.0 | 113 | 103 | 37.0 | 2.00 |
| Ga | 15.1 | 25.7 | 22.6 | 29.4 | 25.9 | 15.1 | 24.7 | 34.0 | 20.8 | 22.6 | 30.4 | 22.2 | 20.6 | 29.0 | 21.1 |
| Rb | 716 | 174 | 724 | 139 | 294 | 566 | 370 | 820 | 1650 | 3390 | 152 | 197 | 337 | 675 | 1290 |
| Sr | 40.6 | 24.4 | 17.1 | 73.3 | 65.0 | 121 | 17.5 | 7.80 | 12.6 | 6.60 | 4.80 | 104 | 70.3 | 6.30 | 12.3 |
| Y | 6.50 | 29.4 | 4.80 | 2.00 | 18.7 | 2.20 | 29.8 | 0.90 | 0.60 | 0.30 | 1.80 | 36.2 | 34.0 | 5.80 | 2.10 |
| Zr | 4.00 | 59.0 | 18.0 | 3.00 | 32.0 | 2.00 | 39.0 | 3.00 | <2 | <2 | 5.00 | 213 | 233 | 11.0 | <2 |
| Nb | 2.00 | 12.7 | 10.4 | 11.8 | 11.2 | 1.00 | 8.40 | 34.8 | 1.30 | 0.30 | 11.2 | 13.5 | 13.2 | 20.0 | 0.50 |
| Mo | 0.50 | 0.84 | 1.14 | 0.73 | 0.40 | 0.50 | 0.83 | 1.28 | 0.34 | 0.34 | 0.63 | 0.66 | 0.41 | 1.02 | 0.34 |
| Cs | 27.1 | 6.94 | 25.6 | 5.57 | 12.8 | 17.2 | 13.4 | 30.8 | 132 | 835 | 8.40 | 25.9 | 74.6 | 29.4 | 41.3 |
| Ba | 40.0 | 15.2 | 34.4 | 9.30 | 41.8 | 181 | 37.7 | 40.4 | 16.2 | 3.50 | 2.70 | 497 | 497 | 11.6 | 14.3 |
| Ta | 0.80 | 3.70 | 2.10 | 1.60 | 1.80 | 0.30 | 1.10 | 3.60 | 0.90 | 0.60 | 1.20 | 1.00 | 1.00 | 4.50 | 0.10 |
| Bi | 0.28 | 0.19 | 0.20 | 0.15 | 0.14 | 0.09 | 0.60 | 0.15 | 18.5 | 3.78 | 8.20 | 0.32 | 0.37 | 12.1 | 0.74 |
| Pb | 65.0 | 19.9 | 32.4 | 19.7 | 37.6 | 84.3 | 46.1 | 20.8 | 57.1 | 62.0 | 17.6 | 28.9 | 21.4 | 38.8 | 57.1 |
| Th | 2.75 | 13.3 | 3.04 | 1.13 | 16.5 | 2.34 | 9.39 | 0.50 | 0.16 | <0.05 | 0.88 | 14.0 | 13.9 | 2.37 | 0.16 |
| U | 1.18 | 4.23 | 0.91 | 0.63 | 2.52 | 0.50 | 4.08 | 0.31 | 0.55 | 0.14 | 1.04 | 2.97 | 2.78 | 2.23 | 0.18 |
| P | 200 | 360 | 200 | 110 | 100 | 110 | 50.0 | 110 | 230 | 190 | 150 | 570 | 430 | 110 | 230 |
| Mn | 55.0 | 156 | 270 | 110 | 97.0 | 44.0 | 178 | 181 | 50.0 | 21.0 | 164 | 899 | 789 | 286 | 63.0 |
| Tl | 4.19 | 0.74 | 4.09 | 0.51 | 1.38 | 3.13 | 1.92 | 4.25 | 10.9 | 25.7 | 0.66 | 0.83 | 1.61 | 3.75 | 7.58 |
| Ag | 0.07 | 0.06 | 0.01 | 0.06 | 0.02 | 0.09 | 0.12 | 0.09 | 0.07 | 0.14 | 0.14 | 0.03 | 0.04 | 0.29 | 0.23 |
| As | 9.40 | 9.70 | 9.90 | 10.9 | 8.90 | 9.90 | 11.2 | 10.9 | 10.2 | 18.3 | 9.50 | 9.70 | 8.90 | 11.1 | 8.80 |
| Ge | 0.14 | 0.16 | 0.14 | 0.13 | 0.13 | 0.15 | 0.17 | 0.16 | 0.11 | 0.12 | 0.12 | 0.23 | 0.24 | 0.17 | 0.13 |
| La | 1.50 | 13.4 | 3.10 | 3.40 | 14.0 | 4.10 | 8.60 | 0.80 | 1.10 | 0.60 | 1.90 | 36.5 | 38.1 | 2.50 | 2.10 |
| Ce | 2.80 | 26.6 | 5.50 | 5.60 | 27.2 | 6.60 | 16.1 | 2.30 | 1.60 | 0.50 | 3.20 | 75.5 | 79.9 | 5.20 | 3.20 |
| Pr | 0.24 | 2.81 | 0.56 | 0.46 | 2.76 | 0.66 | 1.70 | 0.13 | 0.19 | 0.05 | 0.35 | 8.96 | 9.33 | 0.56 | 0.30 |
| Nd | 0.80 | 9.00 | 1.80 | 1.40 | 8.80 | 2.10 | 5.30 | 0.50 | 0.60 | 0.20 | 1.00 | 33.60 | 34.40 | 1.80 | 1.10 |
| Sm | 0.34 | 2.82 | 0.43 | 0.31 | 2.20 | 0.48 | 1.74 | 0.12 | 0.17 | 0.04 | 0.30 | 7.13 | 7.17 | 0.58 | 0.23 |

| | | | | | | | | | | | | | | | |
|---|---|---|---|---|---|---|---|---|---|---|---|---|---|---|---|
| Eu | 0.16 | 0.11 | 0.07 | 0.19 | 0.24 | 0.36 | 0.15 | 0.04 | 0.03 | <0.02 | 0.02 | 1.46 | 1.32 | 0.03 | 0.05 |
| Gd | 0.53 | 3.22 | 0.44 | 0.32 | 2.19 | 0.38 | 2.31 | 0.12 | 0.11 | 0.05 | 0.23 | 6.64 | 6.54 | 0.51 | 0.30 |
| Tb | 0.12 | 0.65 | 0.10 | 0.06 | 0.39 | 0.06 | 0.52 | 0.02 | 0.02 | 0.01 | 0.04 | 1.09 | 1.02 | 0.11 | 0.05 |
| Dy | 0.82 | 4.35 | 0.61 | 0.33 | 2.76 | 0.30 | 3.93 | 0.13 | 0.10 | <0.05 | 0.24 | 6.43 | 6.05 | 0.65 | 0.26 |
| Ho | 0.19 | 0.88 | 0.13 | 0.06 | 0.59 | 0.07 | 0.86 | 0.03 | 0.02 | 0.01 | 0.05 | 1.35 | 1.23 | 0.12 | 0.05 |
| Er | 0.62 | 2.80 | 0.39 | 0.17 | 1.83 | 0.21 | 2.92 | 0.07 | 0.05 | <0.03 | 0.15 | 3.91 | 3.46 | 0.37 | 0.12 |
| Tm | 0.10 | 0.49 | 0.08 | 0.02 | 0.28 | 0.03 | 0.54 | 0.01 | <0.01 | <0.01 | 0.03 | 0.59 | 0.52 | 0.07 | 0.02 |
| Yb | 0.74 | 3.41 | 0.63 | 0.14 | 1.89 | 0.15 | 3.61 | 0.07 | 0.03 | <0.03 | 0.29 | 3.64 | 3.23 | 0.56 | 0.15 |
| Lu | 0.10 | 0.52 | 0.10 | 0.02 | 0.27 | 0.02 | 0.57 | 0.01 | <0.01 | <0.01 | 0.04 | 0.56 | 0.53 | 0.10 | 0.03 |
| Hf | 0.20 | 2.50 | 1.00 | 0.20 | 1.10 | 0.10 | 1.20 | 0.10 | <0.1 | <0.1 | 0.20 | 5.70 | 6.30 | 0.50 | <0.1 |
| LREE | 5.34 | 51.8 | 11.0 | 10.9 | 52.8 | 13.5 | 31.7 | 3.73 | 3.49 | 1.35 | 6.45 | 155 | 162 | 10.1 | 6.70 |
| MREE | 2.16 | 12.0 | 1.78 | 1.27 | 8.37 | 1.65 | 9.51 | 0.46 | 0.45 | 0.11 | 0.88 | 24.1 | 23.3 | 2.00 | 0.94 |
| HREE | 1.76 | 9.72 | 2.20 | 0.55 | 5.37 | 0.51 | 8.84 | 0.26 | 0.08 | 0.00 | 0.71 | 14.4 | 14.0 | 1.60 | 0.32 |
| LREE/HREE | 3.03 | 5.33 | 4.98 | 19.7 | 9.82 | 26.4 | 3.59 | 14.3 | 43.6 | - | 9.08 | 10.7 | 11.5 | 6.29 | 20.9 |
| REE+Y | 15.8 | 103 | 19.7 | 14.7 | 85.2 | 17.8 | 79.9 | 5.35 | 4.62 | 1.76 | 9.84 | 229 | 233 | 19.5 | 10.1 |
| REE | 9.26 | 73.56 | 14.94 | 12.68 | 66.50 | 15.62 | 50.05 | 4.45 | 4.02 | 1.46 | 8.04 | 193 | 199 | 13.7 | 7.96 |
| $(La/Sm)_N$ | 2.78 | 2.99 | 4.53 | 6.90 | 4.00 | 5.37 | 3.11 | 4.19 | 4.07 | 9.44 | 3.98 | 3.22 | 3.34 | 2.71 | 5.74 |
| $(Gd/Yb)_N$ | 0.58 | 0.76 | 0.56 | 1.84 | 0.94 | 2.04 | 0.52 | 1.38 | 2.96 | - | 0.64 | 1.47 | 1.63 | 0.73 | 1.61 |
| $(La/Yb)_N$ | 1.37 | 2.65 | 3.32 | 16.4 | 4.99 | 18.4 | 1.61 | 7.71 | 24.7 | - | 4.42 | 6.76 | 7.95 | 3.01 | 9.44 |
| Ce/Ce* | 1.02 | 0.99 | 0.93 | 0.94 | 0.99 | 0.88 | 0.96 | 1.56 | 0.78 | 0.53 | 0.88 | 0.98 | 0.99 | 1.02 | 0.86 |
| Eu/Eu* | 1.15 | 0.11 | 0.49 | 1.83 | 0.33 | 2.49 | 0.23 | 1.01 | 0.63 | - | 0.22 | 0.64 | 0.58 | 0.17 | 0.58 |

Notes: <: under detection limit; -: beyond number.

*4.3. Compositions of Apatite.*

4.3.1. Major Elements

The major element composition of apatite from the RL-6, RL-10, and RL-16 samples are summarized in Table 3. The apatite from the RL-6 and RL-16 samples has a narrow variation range of 47.39–48.83 wt.% and 47.58–49.99 wt.% $P_2O_5$ content, respectively, and a range of 50.31–51.76 wt.% and 49.18–51.86 wt.% CaO content, respectively. However, the RL-10 sample has a wide variation range of 44.22–49.18 wt.% $P_2O_5$ content and a range of 49.91–54.77 wt.% CaO content. The $Na_2O$ content of apatite from all the samples has the same average content (0.12 wt.% in RL-6, 0.13 wt.% in RL-10, and 0.11 wt.% in RL-16), but RL-16 has a wide variation range of 0.03–0.16 wt.%.

4.3.2. Trace Elements

The trace element composition of apatite from the RL-6, RL-10, and RL-16 samples are shown in Table 4 and plotted in Figures 7 and 8. The total REE (ΣREE) of RL-6 ranges from 3209 to 5179 ppm, and the Eu anomalies are >0.10 (Eu/Eu * = 0.10–0.16). The total REE (ΣREE) of RL-10 ranges from 3381 to 4812 ppm, and the total REE (ΣREE) of RL-16 ranges from 2872 to 7030 ppm. The apatite of RL-10 and RL-16 cannot be distinguished by their respective Eu anomalies (Eu/Eu *) because the Eu anomalies (Eu/Eu *) of almost all the spots are in the range below 0.1. Apatite is enriched in LREEs and depleted in (HREE), and the LREE/HREE ratio ranges from 3.61 to 24.07. The REE patterns of RL-6, RL-10, and RL-16 are generally flat ($(La/Yb)_N$ = 0.78–8.69). In general, the RL-10 apatite has transitional geochemical characteristics between RL-6 and RL-16 apatite. The Y/Ho ratio of RL-6 ranges from 28.41 to 40.58, and RL-16 ranges from 37.51 to 65.45, but RL-10 has a narrow variation range from 30.55 to 32.69 (Figure 8). The Sr content of RL-6, RL-10, and RL-16 decrease in turn, and RL-6 ranges from 59.16 to 77.04; RL-10 ranges from 24.42 to 74.24; and RL-16 ranges from 10.29 to 17.48. Yttrium and high-field-strength element (HFSE; U, Th, Ta, and Hf) content have a wide variation range.

**Table 3.** Major element composition for the apatite from pegmatite of Renli Nb-Ta deposit (wt.%).

| Spot | $Na_2O$ | $P_2O_5$ | $K_2O$ | CaO | $TiO_2$ | Total | Na(apfu) | P(apfu) | K(apfu) | Ca(apfu) | Ti(apfu) | Total |
|---|---|---|---|---|---|---|---|---|---|---|---|---|
| RL-6@1 | 0.12 | 48.24 | 0.00 | 50.95 | 0.00 | 99.30 | 0.02 | 3.38 | 0.00 | 4.53 | 0.00 | 7.93 |
| RL-6@2 | 0.11 | 48.27 | 0.00 | 50.93 | 0.00 | 99.32 | 0.02 | 3.38 | 0.00 | 4.53 | 0.00 | 7.93 |
| RL-6@3 | 0.11 | 48.01 | 0.00 | 51.19 | 0.00 | 99.31 | 0.02 | 3.37 | 0.00 | 4.56 | 0.00 | 7.95 |
| RL-6@4 | 0.12 | 48.28 | 0.00 | 50.91 | 0.00 | 99.31 | 0.02 | 3.39 | 0.00 | 4.53 | 0.00 | 7.93 |
| RL-6@5 | 0.11 | 48.27 | 0.00 | 50.92 | 0.00 | 99.31 | 0.02 | 3.39 | 0.00 | 4.53 | 0.00 | 7.93 |
| RL-6@6 | 0.11 | 48.11 | 0.00 | 51.11 | 0.00 | 99.33 | 0.02 | 3.38 | 0.00 | 4.55 | 0.00 | 7.94 |
| RL-6@7 | 0.13 | 48.16 | 0.00 | 50.88 | 0.00 | 99.18 | 0.02 | 3.38 | 0.00 | 4.53 | 0.00 | 7.94 |
| RL-6@8 | 0.13 | 48.25 | 0.00 | 50.81 | 0.00 | 99.19 | 0.02 | 3.39 | 0.00 | 4.52 | 0.00 | 7.93 |
| RL-6@9 | 0.14 | 48.16 | 0.00 | 50.88 | 0.00 | 99.17 | 0.02 | 3.38 | 0.00 | 4.53 | 0.00 | 7.94 |
| RL-6@10 | 0.12 | 48.14 | 0.00 | 51.04 | 0.00 | 99.30 | 0.02 | 3.38 | 0.00 | 4.54 | 0.00 | 7.94 |
| RL-6@11 | 0.12 | 47.77 | 0.00 | 51.31 | 0.00 | 99.20 | 0.02 | 3.36 | 0.00 | 4.58 | 0.00 | 7.96 |
| RL-6@12 | 0.12 | 47.94 | 0.00 | 51.19 | 0.00 | 99.25 | 0.02 | 3.37 | 0.00 | 4.56 | 0.00 | 7.95 |
| RL-6@13 | 0.11 | 48.22 | 0.00 | 50.95 | 0.00 | 99.28 | 0.02 | 3.38 | 0.00 | 4.53 | 0.00 | 7.93 |
| RL-6@14 | 0.11 | 48.26 | 0.00 | 50.89 | 0.00 | 99.26 | 0.02 | 3.39 | 0.00 | 4.53 | 0.00 | 7.93 |
| RL-6@15 | 0.12 | 47.85 | 0.00 | 51.36 | 0.00 | 99.33 | 0.02 | 3.36 | 0.00 | 4.58 | 0.00 | 7.96 |
| RL-6@16 | 0.12 | 47.75 | 0.00 | 51.37 | 0.00 | 99.24 | 0.02 | 3.36 | 0.00 | 4.59 | 0.00 | 7.97 |
| RL-6@17 | 0.12 | 47.73 | 0.00 | 51.42 | 0.00 | 99.27 | 0.02 | 3.36 | 0.00 | 4.59 | 0.00 | 7.97 |
| RL-6@18 | 0.13 | 48.01 | 0.00 | 51.08 | 0.00 | 99.22 | 0.02 | 3.37 | 0.00 | 4.55 | 0.00 | 7.95 |
| RL-6@19 | 0.14 | 47.62 | 0.00 | 51.38 | 0.00 | 99.13 | 0.02 | 3.36 | 0.00 | 4.59 | 0.00 | 7.97 |
| RL-6@20 | 0.11 | 47.91 | 0.00 | 51.28 | 0.00 | 99.30 | 0.02 | 3.37 | 0.00 | 4.57 | 0.00 | 7.96 |
| RL-6@21 | 0.12 | 48.17 | 0.00 | 51.04 | 0.00 | 99.32 | 0.02 | 3.38 | 0.00 | 4.54 | 0.00 | 7.94 |
| RL-6@22 | 0.11 | 48.16 | 0.00 | 51.00 | 0.00 | 99.27 | 0.02 | 3.38 | 0.00 | 4.54 | 0.00 | 7.94 |
| RL-6@23 | 0.12 | 48.23 | 0.00 | 50.96 | 0.00 | 99.31 | 0.02 | 3.38 | 0.00 | 4.53 | 0.00 | 7.93 |
| RL-6@24 | 0.15 | 48.00 | 0.00 | 50.90 | 0.00 | 99.04 | 0.02 | 3.38 | 0.00 | 4.54 | 0.00 | 7.94 |

| | | | | | | | | | | | | |
|---|---|---|---|---|---|---|---|---|---|---|---|---|
| RL-6@25 | 0.12 | 48.83 | 0.00 | 50.31 | 0.00 | 99.26 | 0.02 | 3.41 | 0.00 | 4.46 | 0.00 | 7.89 |
| RL-6@26 | 0.13 | 48.17 | 0.00 | 50.90 | 0.00 | 99.19 | 0.02 | 3.38 | 0.00 | 4.53 | 0.00 | 7.94 |
| RL-6@27 | 0.12 | 48.26 | 0.00 | 50.82 | 0.00 | 99.21 | 0.02 | 3.39 | 0.00 | 4.52 | 0.00 | 7.93 |
| RL-6@28 | 0.12 | 47.99 | 0.00 | 51.09 | 0.00 | 99.21 | 0.02 | 3.37 | 0.00 | 4.55 | 0.00 | 7.95 |
| RL-6@29 | 0.12 | 48.32 | 0.00 | 50.84 | 0.00 | 99.27 | 0.02 | 3.39 | 0.00 | 4.52 | 0.00 | 7.93 |
| RL-6@30 | 0.12 | 47.93 | 0.00 | 51.22 | 0.00 | 99.27 | 0.02 | 3.37 | 0.00 | 4.57 | 0.00 | 7.95 |
| RL-6@31 | 0.12 | 48.20 | 0.00 | 51.00 | 0.00 | 99.33 | 0.02 | 3.38 | 0.00 | 4.54 | 0.00 | 7.94 |
| RL-6@32 | 0.12 | 48.17 | 0.00 | 50.99 | 0.00 | 99.28 | 0.02 | 3.38 | 0.00 | 4.54 | 0.00 | 7.94 |
| RL-6@33 | 0.13 | 48.16 | 0.00 | 50.92 | 0.00 | 99.21 | 0.02 | 3.38 | 0.00 | 4.53 | 0.00 | 7.94 |
| RL-6@34 | 0.12 | 47.68 | 0.00 | 51.46 | 0.00 | 99.26 | 0.02 | 3.36 | 0.00 | 4.59 | 0.00 | 7.97 |
| RL-6@35 | 0.12 | 47.71 | 0.00 | 51.46 | 0.00 | 99.29 | 0.02 | 3.36 | 0.00 | 4.59 | 0.00 | 7.97 |
| RL-6@36 | 0.14 | 47.71 | 0.00 | 51.18 | 0.00 | 99.03 | 0.02 | 3.36 | 0.00 | 4.58 | 0.00 | 7.96 |
| RL-6@37 | 0.12 | 47.39 | 0.00 | 51.73 | 0.00 | 99.24 | 0.02 | 3.34 | 0.00 | 4.63 | 0.00 | 7.99 |
| RL-6@38 | 0.12 | 47.51 | 0.00 | 51.64 | 0.00 | 99.27 | 0.02 | 3.35 | 0.00 | 4.62 | 0.00 | 7.99 |
| RL-6@39 | 0.12 | 47.55 | 0.00 | 51.60 | 0.00 | 99.27 | 0.02 | 3.35 | 0.00 | 4.61 | 0.00 | 7.98 |
| RL-6@40 | 0.12 | 47.39 | 0.00 | 51.76 | 0.00 | 99.27 | 0.02 | 3.34 | 0.00 | 4.63 | 0.00 | 7.99 |
| RL-6@41 | 0.12 | 48.04 | 0.00 | 51.09 | 0.00 | 99.25 | 0.02 | 3.38 | 0.00 | 4.55 | 0.00 | 7.95 |
| RL-6@42 | 0.12 | 48.32 | 0.00 | 50.85 | 0.00 | 99.30 | 0.02 | 3.39 | 0.00 | 4.52 | 0.00 | 7.93 |
| RL-6@43 | 0.12 | 47.95 | 0.00 | 51.22 | 0.00 | 99.29 | 0.02 | 3.37 | 0.00 | 4.56 | 0.00 | 7.95 |
| RL-6@44 | 0.12 | 48.39 | 0.00 | 50.79 | 0.00 | 99.29 | 0.02 | 3.39 | 0.00 | 4.51 | 0.00 | 7.92 |
| RL-6@45 | 0.12 | 47.78 | 0.00 | 51.35 | 0.00 | 99.24 | 0.02 | 3.36 | 0.00 | 4.58 | 0.00 | 7.96 |
| RL-10@1 | 0.13 | 47.22 | 0.00 | 51.86 | 0.00 | 99.21 | 0.02 | 3.34 | 0.00 | 4.65 | 0.00 | 8.01 |
| RL-10@2 | 0.14 | 47.05 | 0.00 | 52.00 | 0.00 | 99.19 | 0.02 | 3.33 | 0.00 | 4.67 | 0.00 | 8.02 |
| RL-10@3 | 0.14 | 47.31 | 0.00 | 51.73 | 0.00 | 99.18 | 0.02 | 3.34 | 0.00 | 4.63 | 0.00 | 8.00 |
| RL-10@4 | 0.13 | 46.94 | 0.00 | 52.14 | 0.00 | 99.21 | 0.02 | 3.32 | 0.00 | 4.68 | 0.00 | 8.03 |
| RL-10@5 | 0.13 | 47.48 | 0.00 | 51.60 | 0.00 | 99.21 | 0.02 | 3.35 | 0.00 | 4.62 | 0.00 | 7.99 |
| RL-10@6 | 0.14 | 47.40 | 0.00 | 51.68 | 0.00 | 99.22 | 0.02 | 3.35 | 0.00 | 4.62 | 0.00 | 7.99 |
| RL-10@7 | 0.13 | 47.81 | 0.00 | 51.25 | 0.00 | 99.19 | 0.02 | 3.37 | 0.00 | 4.57 | 0.00 | 7.96 |
| RL-10@8 | 0.14 | 47.42 | 0.00 | 51.56 | 0.00 | 99.12 | 0.02 | 3.35 | 0.00 | 4.62 | 0.00 | 7.99 |
| RL-10@9 | 0.13 | 47.76 | 0.00 | 51.32 | 0.00 | 99.22 | 0.02 | 3.36 | 0.00 | 4.58 | 0.00 | 7.97 |
| RL-10@10 | 0.12 | 47.82 | 0.00 | 51.30 | 0.00 | 99.25 | 0.02 | 3.37 | 0.00 | 4.58 | 0.00 | 7.96 |
| RL-10@11 | 0.13 | 47.14 | 0.00 | 51.91 | 0.00 | 99.19 | 0.02 | 3.33 | 0.00 | 4.65 | 0.00 | 8.01 |
| RL-10@12 | 0.12 | 47.57 | 0.00 | 51.54 | 0.00 | 99.23 | 0.02 | 3.35 | 0.00 | 4.61 | 0.00 | 7.98 |
| RL-10@13 | 0.14 | 47.23 | 0.00 | 51.83 | 0.00 | 99.21 | 0.02 | 3.34 | 0.00 | 4.64 | 0.00 | 8.00 |
| RL-10@14 | 0.14 | 47.93 | 0.00 | 51.15 | 0.00 | 99.23 | 0.02 | 3.37 | 0.00 | 4.56 | 0.00 | 7.95 |
| RL-10@15 | 0.14 | 47.74 | 0.00 | 51.30 | 0.00 | 99.18 | 0.02 | 3.36 | 0.00 | 4.58 | 0.00 | 7.97 |
| RL-10@16 | 0.14 | 47.81 | 0.00 | 51.23 | 0.00 | 99.18 | 0.02 | 3.37 | 0.00 | 4.57 | 0.00 | 7.96 |
| RL-10@17 | 0.12 | 47.30 | 0.00 | 51.87 | 0.00 | 99.28 | 0.02 | 3.34 | 0.00 | 4.64 | 0.00 | 8.00 |
| RL-10@18 | 0.13 | 48.03 | 0.00 | 51.05 | 0.00 | 99.21 | 0.02 | 3.38 | 0.00 | 4.55 | 0.00 | 7.95 |
| RL-10@19 | 0.12 | 48.61 | 0.00 | 50.57 | 0.00 | 99.30 | 0.02 | 3.40 | 0.00 | 4.49 | 0.00 | 7.91 |
| RL-10@20 | 0.14 | 44.22 | 0.00 | 54.77 | 0.00 | 99.14 | 0.02 | 3.19 | 0.00 | 5.01 | 0.00 | 8.23 |
| RL-10@21 | 0.12 | 48.46 | 0.00 | 50.68 | 0.00 | 99.27 | 0.02 | 3.40 | 0.00 | 4.50 | 0.00 | 7.92 |
| RL-10@22 | 0.12 | 48.45 | 0.00 | 50.67 | 0.00 | 99.24 | 0.02 | 3.40 | 0.00 | 4.50 | 0.00 | 7.92 |
| RL-10@23 | 0.12 | 48.51 | 0.00 | 50.59 | 0.00 | 99.22 | 0.02 | 3.40 | 0.00 | 4.49 | 0.00 | 7.91 |
| RL-10@24 | 0.13 | 48.51 | 0.00 | 50.58 | 0.00 | 99.22 | 0.02 | 3.40 | 0.00 | 4.49 | 0.00 | 7.91 |
| RL-10@25 | 0.13 | 49.18 | 0.00 | 49.91 | 0.00 | 99.23 | 0.02 | 3.43 | 0.00 | 4.41 | 0.00 | 7.86 |
| RL-16@1 | 0.13 | 49.69 | 0.00 | 49.43 | 0.00 | 99.24 | 0.02 | 3.45 | 0.00 | 4.36 | 0.00 | 7.83 |
| RL-16@2 | 0.13 | 49.58 | 0.00 | 49.53 | 0.00 | 99.24 | 0.02 | 3.45 | 0.00 | 4.37 | 0.00 | 7.84 |
| RL-16@3 | 0.11 | 49.99 | 0.00 | 49.18 | 0.00 | 99.29 | 0.02 | 3.47 | 0.00 | 4.32 | 0.00 | 7.81 |
| RL-16@4 | 0.11 | 49.12 | 0.00 | 50.05 | 0.00 | 99.29 | 0.02 | 3.43 | 0.00 | 4.43 | 0.00 | 7.87 |
| RL-16@5 | 0.13 | 49.67 | 0.00 | 49.48 | 0.00 | 99.28 | 0.02 | 3.45 | 0.00 | 4.36 | 0.00 | 7.83 |
| RL-16@6 | 0.13 | 49.51 | 0.00 | 49.57 | 0.00 | 99.21 | 0.02 | 3.45 | 0.00 | 4.37 | 0.00 | 7.84 |
| RL-16@7 | 0.11 | 49.08 | 0.00 | 50.13 | 0.00 | 99.31 | 0.02 | 3.42 | 0.00 | 4.43 | 0.00 | 7.87 |
| RL-16@8 | 0.13 | 49.69 | 0.00 | 49.42 | 0.00 | 99.24 | 0.02 | 3.45 | 0.00 | 4.36 | 0.00 | 7.83 |
| RL-16@9 | 0.12 | 49.53 | 0.00 | 49.63 | 0.00 | 99.28 | 0.02 | 3.45 | 0.00 | 4.38 | 0.00 | 7.84 |
| RL-16@10 | 0.10 | 49.22 | 0.00 | 50.01 | 0.00 | 99.33 | 0.02 | 3.43 | 0.00 | 4.42 | 0.00 | 7.86 |
| RL-16@11 | 0.04 | 49.21 | 0.00 | 50.45 | 0.00 | 99.71 | 0.01 | 3.42 | 0.00 | 4.45 | 0.00 | 7.87 |

| | | | | | | | | | | | | |
|---|---|---|---|---|---|---|---|---|---|---|---|---|
| RL-16@12 | 0.12 | 48.87 | 0.00 | 50.32 | 0.00 | 99.32 | 0.02 | 3.41 | 0.00 | 4.46 | 0.00 | 7.89 |
| RL-16@13 | 0.13 | 48.73 | 0.00 | 50.33 | 0.00 | 99.19 | 0.02 | 3.41 | 0.00 | 4.46 | 0.00 | 7.90 |
| RL-16@14 | 0.13 | 48.60 | 0.00 | 50.49 | 0.00 | 99.23 | 0.02 | 3.40 | 0.00 | 4.48 | 0.00 | 7.91 |
| RL-16@15 | 0.12 | 48.83 | 0.00 | 50.35 | 0.00 | 99.30 | 0.02 | 3.41 | 0.00 | 4.46 | 0.00 | 7.89 |
| RL-16@16 | 0.12 | 48.28 | 0.00 | 50.86 | 0.00 | 99.27 | 0.02 | 3.39 | 0.00 | 4.52 | 0.00 | 7.93 |
| RL-16@17 | 0.11 | 48.80 | 0.00 | 50.44 | 0.00 | 99.36 | 0.02 | 3.41 | 0.00 | 4.47 | 0.00 | 7.89 |
| RL-16@18 | 0.16 | 49.03 | 0.00 | 49.66 | 0.00 | 98.84 | 0.03 | 3.43 | 0.00 | 4.41 | 0.00 | 7.86 |
| RL-16@19 | 0.12 | 48.17 | 0.00 | 51.01 | 0.00 | 99.30 | 0.02 | 3.38 | 0.00 | 4.54 | 0.00 | 7.94 |
| RL-16@20 | 0.07 | 47.58 | 0.00 | 51.86 | 0.00 | 99.51 | 0.01 | 3.35 | 0.00 | 4.63 | 0.00 | 7.98 |
| RL-16@21 | 0.08 | 48.41 | 0.00 | 50.97 | 0.00 | 99.46 | 0.01 | 3.39 | 0.00 | 4.52 | 0.00 | 7.92 |
| RL-16@22 | 0.11 | 47.99 | 0.00 | 51.16 | 0.00 | 99.26 | 0.02 | 3.37 | 0.00 | 4.56 | 0.00 | 7.95 |
| RL-16@23 | 0.04 | 49.16 | 0.00 | 50.50 | 0.00 | 99.70 | 0.01 | 3.42 | 0.00 | 4.45 | 0.00 | 7.88 |
| RL-16@24 | 0.05 | 48.30 | 0.00 | 51.26 | 0.00 | 99.62 | 0.01 | 3.38 | 0.00 | 4.55 | 0.00 | 7.94 |
| RL-16@25 | 0.12 | 48.38 | 0.00 | 50.70 | 0.00 | 99.20 | 0.02 | 3.39 | 0.00 | 4.51 | 0.00 | 7.92 |
| RL-16@26 | 0.14 | 49.38 | 0.00 | 49.68 | 0.00 | 99.20 | 0.02 | 3.44 | 0.00 | 4.39 | 0.00 | 7.85 |
| RL-16@27 | 0.14 | 49.19 | 0.00 | 49.85 | 0.00 | 99.18 | 0.02 | 3.43 | 0.00 | 4.41 | 0.00 | 7.86 |
| RL-16@28 | 0.12 | 49.20 | 0.00 | 49.99 | 0.00 | 99.30 | 0.02 | 3.43 | 0.00 | 4.42 | 0.00 | 7.87 |
| RL-16@29 | 0.11 | 49.45 | 0.00 | 49.77 | 0.00 | 99.33 | 0.02 | 3.44 | 0.00 | 4.39 | 0.00 | 7.85 |
| RL-16@30 | 0.14 | 49.33 | 0.00 | 49.71 | 0.00 | 99.17 | 0.02 | 3.44 | 0.00 | 4.39 | 0.00 | 7.85 |
| RL-16@31 | 0.13 | 49.34 | 0.00 | 49.77 | 0.00 | 99.23 | 0.02 | 3.44 | 0.00 | 4.40 | 0.00 | 7.85 |
| RL-16@32 | 0.11 | 49.73 | 0.00 | 49.44 | 0.00 | 99.28 | 0.02 | 3.45 | 0.00 | 4.35 | 0.00 | 7.83 |
| RL-16@33 | 0.16 | 49.21 | 0.00 | 49.59 | 0.00 | 98.96 | 0.03 | 3.44 | 0.00 | 4.39 | 0.00 | 7.86 |
| RL-16@34 | 0.16 | 49.54 | 0.00 | 49.25 | 0.00 | 98.94 | 0.03 | 3.45 | 0.00 | 4.35 | 0.00 | 7.83 |
| RL-16@35 | 0.13 | 49.64 | 0.00 | 49.44 | 0.00 | 99.21 | 0.02 | 3.45 | 0.00 | 4.36 | 0.00 | 7.83 |
| RL-16@36 | 0.03 | 49.22 | 0.00 | 50.54 | 0.00 | 99.79 | 0.00 | 3.42 | 0.00 | 4.45 | 0.00 | 7.87 |
| RL-16@37 | 0.12 | 49.17 | 0.00 | 49.99 | 0.00 | 99.28 | 0.02 | 3.43 | 0.00 | 4.42 | 0.00 | 7.87 |
| RL-16@38 | 0.10 | 49.31 | 0.00 | 50.01 | 0.00 | 99.41 | 0.02 | 3.43 | 0.00 | 4.41 | 0.00 | 7.86 |
| RL-16@39 | 0.13 | 49.47 | 0.00 | 49.62 | 0.00 | 99.22 | 0.02 | 3.44 | 0.00 | 4.38 | 0.00 | 7.84 |
| RL-16@40 | 0.11 | 48.31 | 0.00 | 50.85 | 0.00 | 99.28 | 0.02 | 3.39 | 0.00 | 4.52 | 0.00 | 7.93 |

**Table 4.** Trace element composition for apatite of the pegmatite from the Renli Nb-Ta deposit (ppm).

| Spot | Sc | Rb | Sr | Y | La | Ce | Pr | Nd | Sm | Eu | Gd | Tb | Dy | Ho | Er | Tm | Yb | Lu | Hf | Ta | Pb | Th | U | Y/Ho |
|---|---|---|---|---|---|---|---|---|---|---|---|---|---|---|---|---|---|---|---|---|---|---|---|---|
| RL-6@1 | 0.00 | 0.15 | 74.2 | 2268 | 294 | 889 | 124 | 568 | 235 | 11.7 | 297 | 60.2 | 382 | 72.3 | 195 | 28.1 | 179 | 21.9 | 0.19 | 0.04 | 10.1 | 9.0 | 36.4 | 31.4 |
| RL-6@2 | 0.02 | 0.18 | 74.1 | 2235 | 283 | 867 | 120 | 551 | 230 | 11.7 | 298 | 59.7 | 376 | 71.0 | 191 | 27.9 | 177 | 21.9 | 0.22 | 0.04 | 5.9 | 8.5 | 35.4 | 31.5 |
| RL-6@3 | 0.07 | 0.16 | 73.9 | 2244 | 288 | 876 | 121 | 551 | 230 | 11.6 | 299 | 59.9 | 379 | 72.6 | 195 | 28.3 | 179 | 22.2 | 0.20 | 0.03 | 9.7 | 8.7 | 35.7 | 30.9 |
| RL-6@4 | 0.07 | 0.09 | 73.5 | 2235 | 294 | 901 | 124 | 574 | 237 | 11.8 | 302 | 60.1 | 378 | 72.1 | 194 | 28.4 | 180 | 22.5 | 0.12 | 0.04 | 8.8 | 9.2 | 36.9 | 31.0 |
| RL-6@5 | 0.11 | 0.14 | 73.8 | 2201 | 293 | 901 | 123 | 573 | 232 | 11.6 | 300 | 60.2 | 374 | 72.3 | 193 | 28.2 | 179 | 21.7 | 0.19 | 0.03 | 7.2 | 9.4 | 37.4 | 30.4 |
| RL-6@6 | 0.24 | 0.18 | 71.7 | 2223 | 283 | 851 | 115 | 522 | 214 | 12.1 | 276 | 56.9 | 363 | 71.1 | 198 | 29.7 | 193 | 24.5 | 0.17 | 0.03 | 5.1 | 4.3 | 15.0 | 31.3 |
| RL-6@7 | 0.09 | 0.07 | 61.5 | 2478 | 383 | 1160 | 159 | 736 | 291 | 10.5 | 364 | 71.4 | 442 | 85.2 | 223 | 30.9 | 189 | 23.1 | 0.16 | 0.06 | 6.0 | 18.5 | 39.3 | 29.1 |
| RL-6@8 | 0.09 | 0.18 | 64.2 | 2490 | 371 | 1118 | 154 | 708 | 282 | 10.4 | 364 | 70.6 | 437 | 84.1 | 223 | 31.0 | 193 | 23.3 | 0.19 | 0.05 | 7.4 | 17.3 | 35.8 | 29.6 |
| RL-6@9 | 0.31 | 0.16 | 63.3 | 2471 | 395 | 1198 | 165 | 762 | 294 | 10.9 | 375 | 72.3 | 442 | 85.3 | 226 | 31.2 | 191 | 23.3 | 0.18 | 0.03 | 5.0 | 13.8 | 38.0 | 29.0 |
| RL-6@10 | 0.00 | 0.13 | 74.3 | 2255 | 292 | 875 | 120 | 570 | 239 | 11.8 | 308 | 61.9 | 388 | 74.0 | 199 | 28.6 | 185 | 22.8 | 0.14 | 0.05 | 7.0 | 7.2 | 33.2 | 30.5 |
| RL-6@11 | 0.00 | 0.09 | 69.3 | 2442 | 369 | 1118 | 154 | 716 | 277 | 10.7 | 346 | 68.1 | 422 | 81.6 | 215 | 30.9 | 198 | 24.1 | 0.26 | 0.05 | 10.9 | 18.1 | 52.9 | 29.9 |
| RL-6@12 | 0.19 | 0.07 | 69.5 | 2289 | 348 | 1068 | 149 | 680 | 267 | 10.1 | 331 | 64.7 | 405 | 76.9 | 204 | 28.2 | 172 | 20.9 | 0.15 | 0.03 | 7.2 | 12.4 | 41.0 | 29.8 |
| RL-6@13 | 0.21 | 0.16 | 67.7 | 2183 | 332 | 1027 | 142 | 656 | 253 | 9.7 | 308 | 61.0 | 381 | 72.5 | 190 | 26.8 | 161 | 19.2 | 0.12 | 0.04 | 7.5 | 9.7 | 37.2 | 30.1 |
| RL-6@14 | 0.00 | 0.18 | 70.4 | 2367 | 316 | 964 | 132 | 612 | 251 | 12.3 | 320 | 64.3 | 403 | 78.5 | 213 | 31.1 | 200 | 24.7 | 0.19 | 0.04 | 9.0 | 13.2 | 42.8 | 30.1 |
| RL-6@15 | 0.20 | 0.12 | 70.9 | 2063 | 312 | 959 | 133 | 610 | 236 | 9.9 | 293 | 58.1 | 351 | 68.2 | 178 | 25.4 | 159 | 19.1 | 0.14 | 0.04 | 5.9 | 5.3 | 23.0 | 30.3 |
| RL-6@16 | 0.13 | 0.25 | 72.9 | 2490 | 320 | 960 | 130 | 596 | 248 | 14.0 | 316 | 65.2 | 422 | 82.8 | 224 | 34.0 | 221 | 27.6 | 0.20 | 0.05 | 6.9 | 26.1 | 42.5 | 30.1 |
| RL-6@17 | 0.00 | 0.21 | 72.6 | 2366 | 305 | 937 | 131 | 612 | 254 | 10.7 | 318 | 64.2 | 404 | 77.9 | 206 | 29.7 | 187 | 22.8 | 0.12 | 0.05 | 7.7 | 9.9 | 36.9 | 30.4 |
| RL-6@18 | 0.12 | 0.18 | 10.3 | 1980 | 471 | 1441 | 191 | 765 | 426 | 2.1 | 464 | 91.7 | 416 | 48.8 | 90 | 10.4 | 55 | 5.5 | 0.21 | 0.07 | 9.9 | 19.6 | 25.0 | 40.6 |
| RL-6@19 | 0.16 | 0.21 | 68.1 | 2563 | 420 | 1260 | 171 | 784 | 303 | 11.1 | 386 | 75.5 | 467 | 89.8 | 234 | 32.8 | 202 | 24.1 | 0.17 | 0.04 | 9.2 | 30.3 | 59.6 | 28.5 |
| RL-6@20 | 0.08 | 0.11 | 73.0 | 2274 | 296 | 892 | 120 | 553 | 229 | 11.6 | 295 | 60.5 | 382 | 74.2 | 200 | 29.5 | 192 | 24.1 | 0.16 | 0.04 | 7.3 | 9.0 | 37.7 | 30.7 |
| RL-6@21 | 0.14 | 0.20 | 71.5 | 2237 | 294 | 862 | 115 | 527 | 215 | 12.4 | 272 | 55.9 | 366 | 70.7 | 197 | 30.0 | 195 | 24.2 | 0.14 | 0.04 | 8.0 | 8.6 | 32.6 | 31.6 |
| RL-6@22 | 0.19 | 0.11 | 72.1 | 2261 | 326 | 1011 | 137 | 628 | 246 | 11.4 | 302 | 59.8 | 385 | 74.2 | 200 | 29.5 | 190 | 23.5 | 0.19 | 0.04 | 5.9 | 13.0 | 43.1 | 30.5 |
| RL-6@23 | 0.02 | 0.16 | 70.8 | 2177 | 310 | 939 | 128 | 589 | 233 | 10.5 | 292 | 58.2 | 371 | 70.8 | 192 | 28.2 | 179 | 22.3 | 0.19 | 0.05 | 8.5 | 7.6 | 31.6 | 30.8 |
| RL-6@24 | 0.12 | 0.15 | 74.5 | 2636 | 554 | 1572 | 208 | 931 | 339 | 13.8 | 410 | 79.2 | 494 | 92.8 | 241 | 32.7 | 189 | 22.7 | 0.20 | 0.06 | 6.9 | 34.7 | 52.9 | 28.4 |
| RL-6@25 | 0.33 | 0.14 | 71.6 | 2309 | 332 | 1019 | 140 | 633 | 254 | 10.9 | 325 | 63.6 | 400 | 75.9 | 204 | 29.6 | 182 | 22.4 | 0.16 | 0.04 | 6.6 | 12.7 | 45.6 | 30.4 |
| RL-6@26 | 0.00 | 0.27 | 74.1 | 2551 | 331 | 1052 | 145 | 677 | 274 | 12.3 | 347 | 68.6 | 441 | 83.2 | 227 | 34.8 | 232 | 30.4 | 0.17 | 0.03 | 8.1 | 41.9 | 57.2 | 30.7 |
| RL-6@27 | 0.18 | 0.22 | 72.9 | 2462 | 356 | 1076 | 145 | 656 | 267 | 12.6 | 341 | 68.6 | 433 | 81.1 | 217 | 32.0 | 206 | 25.3 | 0.20 | 0.07 | 6.8 | 28.4 | 55.4 | 30.4 |
| RL-6@28 | 0.10 | 0.19 | 77.0 | 2504 | 344 | 1050 | 142 | 644 | 263 | 13.5 | 341 | 69.0 | 439 | 83.3 | 225 | 33.2 | 213 | 25.8 | 0.14 | 0.05 | 8.9 | 31.5 | 56.6 | 30.1 |
| RL-6@29 | 0.16 | 0.19 | 73.4 | 2367 | 304 | 921 | 127 | 585 | 249 | 12.2 | 319 | 64.0 | 407 | 77.3 | 206 | 31.0 | 196 | 24.4 | 0.17 | 0.04 | 7.5 | 13.4 | 45.9 | 30.6 |
| RL-6@30 | 0.00 | 0.13 | 74.1 | 2265 | 335 | 1002 | 139 | 639 | 247 | 12.5 | 305 | 60.7 | 382 | 73.3 | 197 | 28.4 | 178 | 21.7 | 0.16 | 0.02 | 7.2 | 9.4 | 34.2 | 30.9 |
| RL-6@31 | 0.00 | 0.15 | 74.3 | 2168 | 296 | 874 | 120 | 551 | 230 | 11.8 | 290 | 59.2 | 372 | 69.9 | 187 | 27.8 | 178 | 22.0 | 0.12 | 0.04 | 7.5 | 4.9 | 22.5 | 31.0 |

| | | | | | | | | | | | | | | | | | | | | | | | |
|---|---|---|---|---|---|---|---|---|---|---|---|---|---|---|---|---|---|---|---|---|---|---|---|
| RL-6@32 | 0.06 | 0.16 | 73.3 | 2247 | 321 | 999 | 136 | 625 | 248 | 11.4 | 311 | 62.0 | 391 | 73.7 | 201 | 29.6 | 185 | 22.5 | 0.18 | 0.05 | 7.7 | 12.4 | 42.6 | 30.5 |
| RL-6@33 | 0.00 | 0.15 | 67.6 | 2253 | 426 | 1258 | 170 | 758 | 277 | 11.1 | 337 | 64.9 | 400 | 76.5 | 201 | 27.7 | 164 | 19.8 | 0.13 | 0.05 | 7.1 | 15.6 | 42.6 | 29.5 |
| RL-6@34 | 0.32 | 0.12 | 71.0 | 2237 | 338 | 1064 | 146 | 668 | 262 | 10.5 | 324 | 63.3 | 396 | 75.2 | 198 | 27.9 | 170 | 20.7 | 0.13 | 0.04 | 7.4 | 11.8 | 42.0 | 29.7 |
| RL-6@35 | 1.06 | 0.18 | 70.6 | 2211 | 324 | 997 | 138 | 621 | 249 | 10.0 | 312 | 61.1 | 381 | 73.9 | 194 | 27.1 | 167 | 19.7 | 0.21 | 0.07 | 7.2 | 8.2 | 36.3 | 29.9 |
| RL-6@36 | 0.05 | 0.16 | 59.2 | 3196 | 416 | 1267 | 172 | 745 | 305 | 10.7 | 372 | 80.1 | 524 | 100.0 | 286 | 45.8 | 310 | 38.9 | 0.16 | 0.04 | 5.4 | 47.9 | 76.5 | 32.0 |
| RL-6@37 | 0.01 | 0.18 | 76.9 | 2384 | 369 | 1056 | 141 | 637 | 255 | 12.7 | 321 | 64.3 | 403 | 77.8 | 209 | 31.0 | 202 | 24.7 | 0.17 | 0.04 | 6.4 | 10.3 | 38.2 | 30.6 |
| RL-6@38 | 0.07 | 0.20 | 71.1 | 2309 | 316 | 985 | 135 | 613 | 245 | 10.2 | 315 | 63.2 | 398 | 76.2 | 206 | 30.2 | 189 | 23.0 | 0.16 | 0.03 | 8.4 | 10.4 | 39.3 | 30.3 |
| RL-6@39 | 0.00 | 0.24 | 75.1 | 2244 | 333 | 1022 | 142 | 648 | 254 | 11.7 | 319 | 63.4 | 396 | 74.1 | 198 | 27.7 | 168 | 20.3 | 0.22 | 0.05 | 7.6 | 9.8 | 37.9 | 30.3 |
| RL-6@40 | 0.00 | 0.12 | 74.4 | 2376 | 297 | 908 | 124 | 569 | 237 | 11.9 | 304 | 62.0 | 400 | 78.0 | 216 | 32.8 | 222 | 28.3 | 0.14 | 0.04 | 8.7 | 11.3 | 40.8 | 30.5 |
| RL-6@41 | 0.00 | 0.13 | 76.3 | 2346 | 327 | 1008 | 140 | 641 | 264 | 12.3 | 335 | 66.1 | 411 | 78.2 | 207 | 29.4 | 186 | 22.4 | 0.19 | 0.13 | 7.5 | 15.5 | 46.7 | 30.0 |
| RL-6@42 | 0.01 | 0.13 | 75.5 | 2146 | 328 | 1006 | 138 | 622 | 246 | 12.1 | 306 | 59.9 | 372 | 70.3 | 189 | 26.5 | 163 | 19.8 | 0.17 | 0.03 | 6.9 | 8.6 | 34.4 | 30.5 |
| RL-6@43 | 0.10 | 0.15 | 72.6 | 2353 | 296 | 897 | 122 | 553 | 232 | 12.2 | 302 | 62.5 | 400 | 77.0 | 210 | 31.7 | 204 | 25.0 | 0.20 | 0.04 | 9.0 | 9.7 | 32.5 | 30.6 |
| RL-6@44 | 0.00 | 0.13 | 70.6 | 2316 | 302 | 920 | 124 | 563 | 227 | 11.7 | 296 | 59.7 | 386 | 75.5 | 207 | 31.2 | 203 | 25.2 | 0.23 | 0.04 | 5.9 | 9.5 | 31.9 | 30.7 |
| RL-6@45 | 0.12 | 0.21 | 76.8 | 2332 | 375 | 1067 | 142 | 651 | 255 | 13.6 | 316 | 62.4 | 396 | 76.2 | 204 | 30.0 | 192 | 23.5 | 0.19 | 0.03 | 6.3 | 11.3 | 32.7 | 30.6 |
| RL-10@1 | 0.00 | 0.11 | 27.0 | 2540 | 297 | 949 | 142 | 671 | 345 | 6.3 | 416 | 83.0 | 478 | 80.8 | 206 | 29.9 | 192 | 23.2 | 0.23 | 0.04 | 8.6 | 5.5 | 20.9 | 31.4 |
| RL-10@2 | 0.14 | 0.16 | 37.2 | 2634 | 306 | 956 | 143 | 693 | 338 | 6.2 | 423 | 84.7 | 494 | 85.2 | 218 | 32.5 | 206 | 25.3 | 0.26 | 0.05 | 8.0 | 5.9 | 24.7 | 30.9 |
| RL-10@3 | 0.12 | 0.16 | 37.7 | 2666 | 310 | 969 | 145 | 698 | 344 | 5.9 | 420 | 85.4 | 497 | 84.9 | 219 | 32.3 | 208 | 25.5 | 0.19 | 0.05 | 8.8 | 6.0 | 29.4 | 31.4 |
| RL-10@4 | 0.10 | 0.19 | 27.0 | 2451 | 304 | 1008 | 152 | 724 | 356 | 5.5 | 418 | 82.1 | 468 | 78.5 | 197 | 28.4 | 179 | 21.4 | 0.22 | 0.05 | 8.2 | 6.4 | 7.1 | 31.2 |
| RL-10@5 | 0.10 | 0.20 | 27.1 | 2470 | 305 | 1015 | 153 | 720 | 355 | 5.6 | 417 | 82.0 | 472 | 77.8 | 196 | 28.3 | 177 | 21.4 | 0.27 | 0.04 | 5.8 | 6.6 | 17.7 | 31.7 |
| RL-10@6 | 0.19 | 0.15 | 26.6 | 2666 | 265 | 837 | 127 | 603 | 348 | 5.8 | 415 | 85.7 | 496 | 83.6 | 220 | 33.4 | 225 | 27.7 | 0.20 | 0.06 | 7.8 | 4.5 | 12.0 | 31.9 |
| RL-10@7 | 0.18 | 0.16 | 26.7 | 2629 | 308 | 969 | 144 | 691 | 355 | 6.6 | 428 | 85.3 | 493 | 84.3 | 218 | 31.9 | 203 | 24.7 | 0.18 | 0.03 | 9.3 | 6.8 | 22.8 | 31.2 |
| RL-10@8 | 0.08 | 0.13 | 28.2 | 2465 | 472 | 1456 | 206 | 863 | 365 | 5.8 | 390 | 78.2 | 448 | 75.7 | 199 | 30.0 | 200 | 24.1 | 0.18 | 0.05 | 7.7 | 7.7 | 13.1 | 32.6 |
| RL-10@9 | 0.00 | 0.09 | 26.9 | 2594 | 287 | 898 | 132 | 611 | 354 | 7.2 | 446 | 88.2 | 494 | 80.6 | 203 | 29.5 | 186 | 22.5 | 0.22 | 0.04 | 8.6 | 4.0 | 14.8 | 32.2 |
| RL-10@10 | 0.06 | 0.16 | 27.0 | 2517 | 283 | 854 | 123 | 571 | 316 | 6.9 | 396 | 80.0 | 468 | 79.6 | 208 | 30.5 | 200 | 24.9 | 0.26 | 0.05 | 5.8 | 4.6 | 7.5 | 31.6 |
| RL-10@11 | 0.00 | 0.23 | 52.9 | 2702 | 297 | 943 | 141 | 670 | 339 | 6.2 | 416 | 83.5 | 488 | 83.1 | 217 | 31.5 | 205 | 25.4 | 0.22 | 0.05 | 7.7 | 5.3 | 22.2 | 32.5 |
| RL-10@12 | 0.12 | 0.16 | 74.2 | 2474 | 297 | 962 | 138 | 645 | 325 | 6.2 | 390 | 76.9 | 450 | 77.4 | 202 | 28.6 | 184 | 23.2 | 0.23 | 0.04 | 7.7 | 4.8 | 18.8 | 31.9 |
| RL-10@13 | 0.28 | 0.17 | 27.8 | 2582 | 301 | 968 | 144 | 680 | 334 | 5.8 | 401 | 80.4 | 471 | 82.4 | 214 | 31.3 | 202 | 24.9 | 0.18 | 0.05 | 7.7 | 3.7 | 13.6 | 31.3 |
| RL-10@14 | 0.02 | 0.15 | 29.6 | 2556 | 283 | 897 | 134 | 639 | 330 | 6.2 | 404 | 81.2 | 473 | 80.8 | 210 | 31.0 | 202 | 25.0 | 0.20 | 0.04 | 8.3 | 2.7 | 11.2 | 31.6 |
| RL-10@15 | 0.26 | 0.20 | 27.4 | 2626 | 306 | 1002 | 149 | 704 | 344 | 6.0 | 418 | 82.2 | 488 | 84.8 | 221 | 31.7 | 204 | 24.8 | 0.16 | 0.06 | 8.0 | 4.9 | 17.9 | 31.0 |
| RL-10@16 | 0.01 | 0.23 | 27.8 | 2679 | 308 | 995 | 150 | 705 | 342 | 6.1 | 420 | 83.7 | 495 | 85.8 | 222 | 32.3 | 204 | 24.8 | 0.23 | 0.04 | 8.2 | 5.0 | 17.3 | 31.2 |
| RL-10@17 | 0.02 | 0.21 | 28.2 | 2245 | 249 | 875 | 135 | 646 | 357 | 5.4 | 414 | 80.7 | 443 | 69.4 | 169 | 24.2 | 150 | 16.8 | 0.22 | 0.03 | 7.9 | 6.2 | 10.5 | 32.3 |
| RL-10@18 | 0.21 | 0.16 | 24.4 | 2594 | 289 | 901 | 130 | 597 | 375 | 6.7 | 479 | 95.2 | 509 | 79.4 | 194 | 28.0 | 176 | 21.8 | 0.16 | 0.04 | 4.7 | 5.8 | 15.2 | 32.7 |
| RL-10@19 | 0.29 | 0.17 | 28.8 | 2385 | 271 | 811 | 112 | 510 | 282 | 6.8 | 352 | 73.2 | 435 | 75.2 | 199 | 30.1 | 200 | 25.0 | 0.26 | 0.05 | 8.6 | 5.8 | 7.9 | 31.7 |

| | | | | | | | | | | | | | | | | | | | | | | | |
|---|---|---|---|---|---|---|---|---|---|---|---|---|---|---|---|---|---|---|---|---|---|---|---|
| RL-10@20 | 0.00 | 0.19 | 29.2 | 2930 | 315 | 922 | 136 | 666 | 361 | 7.7 | 461 | 93.0 | 547 | 95.9 | 249 | 36.2 | 232 | 28.8 | 0.19 | 0.03 | 10.1 | 7.9 | 17.9 | 30.6 |
| RL-10@21 | 0.12 | 0.13 | 25.3 | 2471 | 231 | 782 | 119 | 566 | 336 | 7.1 | 422 | 84.6 | 473 | 77.7 | 194 | 28.0 | 174 | 21.1 | 0.17 | 0.05 | 6.4 | 3.8 | 9.3 | 31.8 |
| RL-10@22 | 0.00 | 0.12 | 25.8 | 2332 | 299 | 985 | 149 | 709 | 351 | 5.2 | 404 | 78.9 | 451 | 75.6 | 191 | 26.9 | 168 | 20.3 | 0.16 | 0.05 | 8.6 | 6.4 | 18.1 | 30.8 |
| RL-10@23 | 0.07 | 0.16 | 25.6 | 2450 | 300 | 987 | 149 | 701 | 350 | 5.5 | 410 | 80.6 | 466 | 78.2 | 198 | 28.3 | 177 | 21.4 | 0.21 | 0.04 | 9.8 | 6.3 | 16.1 | 31.3 |
| RL-10@24 | 0.15 | 0.12 | 25.9 | 2653 | 256 | 814 | 124 | 604 | 346 | 5.9 | 405 | 84.7 | 491 | 83.0 | 218 | 33.4 | 220 | 26.8 | 0.24 | 0.05 | 8.8 | 4.6 | 11.6 | 31.9 |
| RL-10@25 | 0.14 | 0.09 | 25.2 | 2488 | 295 | 934 | 139 | 661 | 337 | 6.0 | 401 | 80.0 | 472 | 79.8 | 203 | 29.5 | 188 | 23.0 | 0.14 | 0.04 | 7.1 | 5.6 | 22.5 | 31.2 |
| RL-16@1 | 0.00 | 0.13 | 11.2 | 1886 | 479 | 1421 | 189 | 744 | 405 | 2.0 | 440 | 88.2 | 399 | 46.9 | 87 | 10.2 | 53 | 5.2 | 0.24 | 0.02 | 8.4 | 19.1 | 24.4 | 40.2 |
| RL-16@2 | 0.04 | 0.12 | 11.1 | 1872 | 486 | 1435 | 190 | 753 | 405 | 2.0 | 443 | 88.1 | 399 | 46.2 | 87 | 10.1 | 53 | 5.2 | 0.16 | 0.07 | 10.4 | 20.1 | 25.5 | 40.5 |
| RL-16@3 | 0.04 | 0.06 | 11.8 | 1708 | 455 | 1381 | 181 | 692 | 377 | 2.1 | 399 | 80.3 | 362 | 41.9 | 77 | 9.0 | 45 | 4.5 | 0.16 | 0.02 | 12.6 | 20.1 | 29.9 | 40.8 |
| RL-16@4 | 0.00 | 0.06 | 11.5 | 1667 | 502 | 1432 | 185 | 702 | 376 | 2.3 | 400 | 79.7 | 353 | 40.3 | 74 | 8.8 | 43 | 4.3 | 0.20 | 0.02 | 10.5 | 16.7 | 23.2 | 41.4 |
| RL-16@5 | 0.03 | 0.00 | 10.3 | 1884 | 392 | 1262 | 173 | 705 | 402 | 2.0 | 447 | 88.5 | 401 | 46.7 | 87 | 9.9 | 52 | 5.0 | 0.16 | 0.03 | 10.2 | 12.1 | 17.6 | 40.4 |
| RL-16@6 | 0.09 | 0.07 | 11.0 | 1979 | 490 | 1469 | 197 | 774 | 429 | 2.2 | 460 | 90.7 | 416 | 48.3 | 89 | 10.6 | 56 | 5.6 | 0.13 | 0.02 | 9.9 | 18.2 | 23.4 | 41.0 |
| RL-16@7 | 0.04 | 0.00 | 12.0 | 1598 | 474 | 1375 | 180 | 684 | 359 | 2.3 | 390 | 76.5 | 348 | 40.9 | 75 | 8.7 | 44 | 4.4 | 0.16 | 0.02 | 8.5 | 17.3 | 21.6 | 39.1 |
| RL-16@8 | 0.06 | 0.13 | 11.1 | 1861 | 486 | 1458 | 191 | 740 | 396 | 2.1 | 429 | 86.4 | 396 | 46.0 | 87 | 10.0 | 54 | 5.2 | 0.17 | 0.02 | 10.3 | 20.2 | 23.7 | 40.5 |
| RL-16@9 | 0.00 | 0.06 | 11.4 | 1683 | 470 | 1411 | 187 | 725 | 391 | 2.0 | 428 | 83.4 | 378 | 42.8 | 77 | 8.8 | 44 | 4.5 | 0.16 | 0.03 | 10.2 | 18.6 | 23.9 | 39.4 |
| RL-16@10 | 0.00 | 0.00 | 11.8 | 1580 | 513 | 1419 | 170 | 570 | 284 | 2.7 | 281 | 62.1 | 302 | 35.6 | 72 | 9.5 | 54 | 5.4 | 0.03 | 0.00 | 13.0 | 143.8 | 61.0 | 44.4 |
| RL-16@11 | 0.00 | 0.09 | 16.3 | 456 | 433 | 900 | 84 | 222 | 86 | 3.8 | 70 | 15.6 | 72 | 7.6 | 15 | 1.9 | 10 | 1.0 | 0.15 | 0.02 | 14.7 | 15.9 | 15.0 | 59.9 |
| RL-16@12 | 0.00 | 0.03 | 11.2 | 1634 | 434 | 1319 | 174 | 680 | 375 | 2.0 | 414 | 80.1 | 365 | 41.9 | 77 | 8.7 | 44 | 4.3 | 0.11 | 0.04 | 11.2 | 9.6 | 18.0 | 39.0 |
| RL-16@13 | 0.04 | 0.03 | 11.2 | 2027 | 485 | 1458 | 195 | 779 | 435 | 1.9 | 488 | 96.0 | 436 | 51.5 | 99 | 11.3 | 60 | 5.8 | 0.13 | 0.03 | 16.0 | 18.4 | 23.6 | 39.3 |
| RL-16@14 | 0.06 | 0.00 | 11.7 | 1876 | 495 | 1502 | 196 | 766 | 410 | 2.4 | 442 | 87.9 | 409 | 47.0 | 87 | 10.6 | 54 | 5.3 | 0.17 | 0.02 | 9.5 | 18.1 | 22.4 | 39.9 |
| RL-16@15 | 0.00 | 0.08 | 12.0 | 1632 | 466 | 1396 | 182 | 699 | 379 | 2.1 | 410 | 80.2 | 360 | 41.9 | 78 | 8.7 | 46 | 4.3 | 0.19 | 0.02 | 11.7 | 16.9 | 23.2 | 39.0 |
| RL-16@16 | 0.00 | 0.00 | 11.6 | 1752 | 466 | 1397 | 184 | 730 | 407 | 2.0 | 443 | 86.5 | 389 | 44.6 | 83 | 9.3 | 48 | 4.5 | 0.12 | 0.02 | 10.4 | 13.8 | 21.0 | 39.3 |
| RL-16@17 | 0.05 | 0.20 | 11.3 | 1550 | 400 | 1242 | 162 | 633 | 357 | 2.0 | 385 | 75.6 | 338 | 38.8 | 71 | 7.8 | 41 | 3.9 | 0.28 | 0.10 | 9.5 | 9.4 | 16.8 | 39.9 |
| RL-16@18 | 0.00 | 0.03 | 13.2 | 2572 | 829 | 2443 | 322 | 1183 | 628 | 3.8 | 642 | 130.6 | 586 | 65.1 | 115 | 12.9 | 64 | 6.1 | 0.19 | 0.02 | 11.8 | 21.7 | 25.7 | 39.5 |
| RL-16@19 | 0.06 | 0.00 | 11.1 | 1730 | 421 | 1313 | 173 | 690 | 381 | 2.1 | 414 | 82.1 | 370 | 42.8 | 80 | 9.4 | 48 | 4.5 | 0.14 | 0.03 | 9.6 | 11.5 | 19.1 | 40.4 |
| RL-16@20 | 0.00 | 0.05 | 13.3 | 1168 | 347 | 1066 | 133 | 462 | 230 | 2.6 | 225 | 49.4 | 234 | 27.4 | 52 | 6.5 | 34 | 3.3 | 0.10 | 0.03 | 8.2 | 9.2 | 29.4 | 42.7 |
| RL-16@21 | 0.00 | 0.07 | 13.2 | 1309 | 364 | 1145 | 140 | 484 | 245 | 2.5 | 244 | 53.5 | 259 | 30.3 | 60 | 7.7 | 40 | 3.9 | 0.16 | 0.04 | 8.1 | 14.2 | 44.2 | 43.2 |
| RL-16@22 | 0.14 | 0.00 | 12.3 | 1737 | 481 | 1424 | 186 | 741 | 414 | 2.4 | 451 | 87.2 | 392 | 44.8 | 82 | 9.3 | 47 | 4.4 | 0.01 | 0.00 | 11.8 | 15.0 | 19.5 | 38.8 |
| RL-16@23 | 0.00 | 0.00 | 14.0 | 109 | 514 | 1141 | 111 | 306 | 108 | 2.7 | 73 | 10.6 | 31 | 2.1 | 2 | 0.2 | 1 | 0.1 | 0.04 | 0.00 | 13.7 | 40.6 | 24.9 | 52.9 |
| RL-16@24 | 0.00 | 0.04 | 15.3 | 251 | 562 | 1345 | 144 | 446 | 167 | 3.2 | 122 | 19.2 | 69 | 5.5 | 8 | 0.8 | 4 | 0.3 | 0.15 | 0.03 | 11.9 | 19.9 | 17.7 | 45.6 |
| RL-16@25 | 0.00 | 0.06 | 11.1 | 2027 | 493 | 1473 | 199 | 777 | 431 | 2.2 | 477 | 93.6 | 433 | 50.1 | 95 | 10.7 | 56 | 5.8 | 0.23 | 0.03 | 11.9 | 18.5 | 30.3 | 40.4 |
| RL-16@26 | 0.00 | 0.10 | 10.8 | 1957 | 477 | 1473 | 200 | 803 | 445 | 2.1 | 492 | 95.1 | 431 | 50.0 | 92 | 10.6 | 55 | 5.4 | 0.19 | 0.03 | 9.3 | 17.6 | 21.3 | 39.1 |
| RL-16@27 | 0.18 | 0.06 | 11.0 | 2072 | 473 | 1487 | 199 | 793 | 448 | 2.0 | 495 | 95.9 | 442 | 52.6 | 100 | 11.8 | 62 | 6.2 | 0.17 | 0.02 | 9.2 | 18.1 | 22.1 | 39.4 |
| RL-16@28 | 0.00 | 0.07 | 11.9 | 1591 | 482 | 1418 | 182 | 699 | 380 | 2.0 | 415 | 78.9 | 353 | 41.3 | 77 | 8.9 | 46 | 4.4 | 0.18 | 0.03 | 10.9 | 18.0 | 24.1 | 38.5 |

| | | | | | | | | | | | | | | | | | | | | | | | |
|---|---|---|---|---|---|---|---|---|---|---|---|---|---|---|---|---|---|---|---|---|---|---|---|
| RL-16@29 | 0.16 | 0.24 | 11.7 | 1553 | 438 | 1334 | 175 | 669 | 365 | 2.2 | 399 | 76.7 | 346 | 40.5 | 73 | 8.4 | 42 | 4.1 | 0.16 | 0.03 | 10.1 | 11.3 | 18.3 | 38.4 |
| RL-16@30 | 0.00 | 0.09 | 11.8 | 1977 | 581 | 1694 | 215 | 787 | 423 | 2.8 | 439 | 90.4 | 408 | 46.3 | 84 | 9.7 | 50 | 4.8 | 0.18 | 0.03 | 7.6 | 21.1 | 25.4 | 42.7 |
| RL-16@31 | 0.03 | 0.09 | 11.3 | 1877 | 477 | 1476 | 195 | 748 | 405 | 2.1 | 440 | 87.2 | 398 | 46.1 | 86 | 10.0 | 54 | 5.2 | 0.21 | 0.02 | 10.4 | 19.5 | 24.6 | 40.7 |
| RL-16@32 | 0.00 | 0.00 | 12.0 | 1661 | 462 | 1401 | 185 | 718 | 391 | 2.1 | 430 | 83.9 | 372 | 44.3 | 82 | 9.3 | 48 | 4.7 | 0.27 | 0.03 | 12.6 | 16.0 | 21.6 | 37.5 |
| RL-16@33 | 0.00 | 0.01 | 12.0 | 2376 | 780 | 2190 | 283 | 1016 | 535 | 3.4 | 555 | 115.0 | 516 | 58.0 | 106 | 12.0 | 62 | 5.8 | 0.21 | 0.05 | 9.6 | 37.5 | 31.9 | 41.0 |
| RL-16@34 | 0.15 | 0.13 | 12.1 | 2386 | 780 | 2208 | 287 | 1050 | 556 | 3.6 | 576 | 119.4 | 536 | 59.9 | 107 | 12.2 | 62 | 6.0 | 0.16 | 0.03 | 12.3 | 34.3 | 30.8 | 39.8 |
| RL-16@35 | 0.06 | 0.00 | 11.2 | 1969 | 460 | 1451 | 196 | 771 | 423 | 2.0 | 469 | 92.9 | 425 | 51.0 | 96 | 11.2 | 60 | 6.0 | 0.02 | 0.00 | 10.1 | 16.4 | 20.2 | 38.6 |
| RL-16@36 | 0.05 | 0.05 | 17.5 | 212 | 367 | 669 | 54 | 122 | 41 | 4.5 | 27 | 6.1 | 29 | 3.2 | 7 | 1.1 | 8 | 0.9 | 0.15 | 0.03 | 12.0 | 88.8 | 33.8 | 65.5 |
| RL-16@37 | 0.00 | 0.06 | 10.8 | 1802 | 445 | 1374 | 183 | 699 | 385 | 2.0 | 413 | 82.6 | 381 | 44.2 | 82 | 9.7 | 51 | 4.9 | 0.11 | 0.02 | 12.3 | 18.8 | 27.2 | 40.8 |
| RL-16@38 | 0.01 | 0.02 | 10.7 | 1465 | 417 | 1230 | 151 | 521 | 266 | 2.1 | 266 | 57.8 | 278 | 32.9 | 65 | 8.3 | 46 | 4.5 | 0.19 | 0.03 | 12.0 | 19.6 | 33.4 | 44.6 |
| RL-16@39 | 0.19 | 0.06 | 11.0 | 1984 | 472 | 1443 | 193 | 758 | 411 | 2.1 | 455 | 90.3 | 423 | 49.9 | 96 | 11.4 | 61 | 6.0 | 0.16 | 0.04 | 9.3 | 13.9 | 20.4 | 39.8 |
| RL-16@40 | 0.00 | 0.15 | 11.8 | 1664 | 488 | 1424 | 183 | 721 | 396 | 2.3 | 427 | 82.6 | 374 | 43.2 | 78 | 8.6 | 44 | 4.3 | 0.19 | 0.04 | 11.3 | 19.7 | 24.9 | 38.5 |

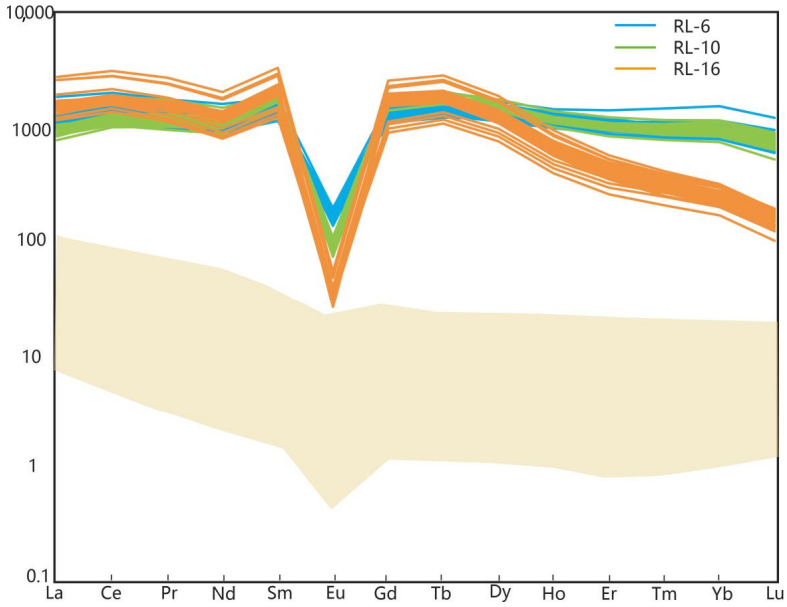


**Figure 7.** Chondrite-normalized REE patterns of apatite from the RL-6, RL-10, and RL-16 samples [36]. Pale yellow area is the REE pattern of host pegmatite.

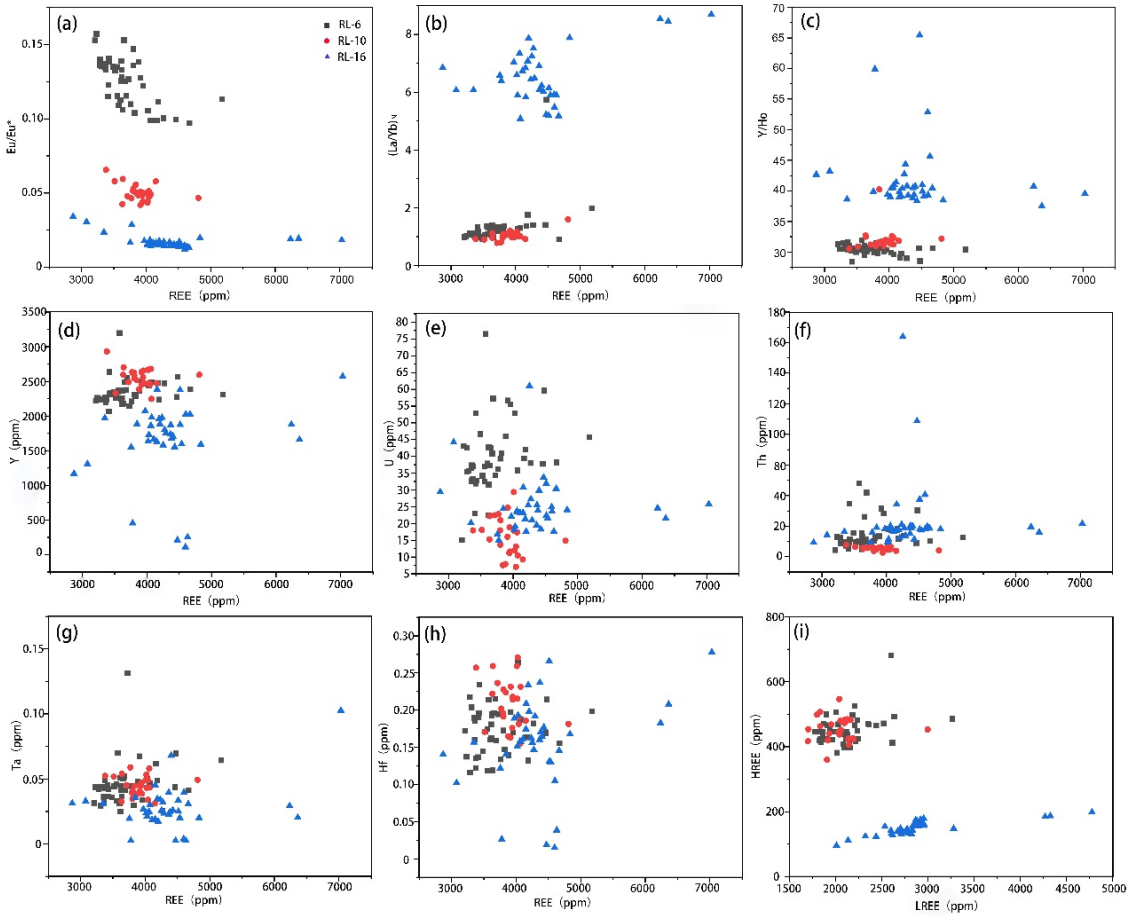


**Figure 8.** Scatter diagram of apatite in the RL-6, RL-10, and RL-16 samples: (**a**) REE vs. Eu/Eu *; (**b**) REE vs. $(La/Yb)_N$; (**c**) REE vs. Y/Ho; (**d**) REE vs. Y; (**e**) REE vs. U; (**f**) REE vs. Th; (**g**) REE vs. Ta; (**h**) REE vs. Hf; and (**i**) LREE vs. HREE.

### *4.4. Apatite U-Pb Ages*

The results of apatite U-Pb dating are listed in Table 5 and plotted in Figure 9. There are 45 spots along a discordia in the Tera–Wasserburg Concordia diagram of RL-6, and they yield a lower intercept age of 130 ± 2 Ma (2σ, MSWD = 1.2, Figure 9a, [37]). There are 25 spots along a discordia in the Tera–Wasserburg Concordia diagram of RL-10, and they yield a lower intercept age of 135 ± 8 Ma (2σ, MSWD = 1.8, Figure 9b, [37]). There are 40 spots along a discordia in the Tera–Wasserburg Concordia diagram of RL-16, and they yield a lower intercept age of 134 ± 3 Ma (2σ, MSWD = 1.3, Figure 9c, [37]).

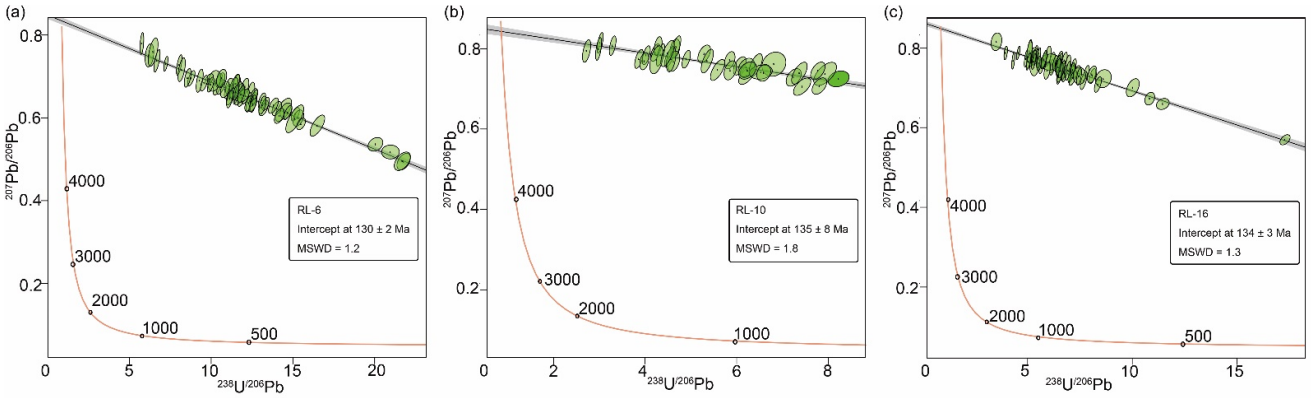


**Figure 9.** Apatite U-Pb lower intercept ages of the (**a**) RL-6, (**b**) RL-10, and (**c**) RL-16 samples.

**Table 5.** Apatite U-Pb dating by LA-ICP-MS.

| Sample | U (ppm) | 2s Error | Th (ppm) | 2s Error | $^{207}Pb/^{206}Pb$ | 2s Error | $^{206}Pb/^{238}U$ | 2s Error | $^{207}Pb/^{235}U$ | 2s Error | $^{206}Pb/^{238}U$ Age | ± | 2σ (Ma) |
|---|---|---|---|---|---|---|---|---|---|---|---|---|---|
| RL-6 | | | | | | | | | | | | | |
| RL-6@1 | 34.6 | 0.3 | 13.1 | 0.3 | 0.66 | 0.01 | 0.09 | 0.00 | 8.10 | 0.13 | 544 | ± | 8 |
| RL-6@2 | 33.9 | 0.3 | 12.6 | 0.3 | 0.66 | 0.01 | 0.09 | 0.00 | 8.40 | 0.15 | 560 | ± | 9 |
| RL-6@3 | 34.5 | 0.2 | 12.7 | 0.3 | 0.65 | 0.01 | 0.09 | 0.00 | 8.04 | 0.15 | 553 | ± | 7 |
| RL-6@4 | 35.6 | 0.2 | 13.6 | 0.3 | 0.68 | 0.02 | 0.09 | 0.00 | 8.13 | 0.18 | 536 | ± | 8 |
| RL-6@5 | 35.7 | 0.3 | 13.6 | 0.3 | 0.65 | 0.01 | 0.09 | 0.00 | 7.80 | 0.15 | 538 | ± | 6 |
| RL-6@6 | 14.1 | 0.2 | 6.0 | 0.2 | 0.78 | 0.02 | 0.17 | 0.00 | 18.58 | 0.46 | 1030 | ± | 14 |
| RL-6@7 | 35.5 | 0.4 | 25.6 | 0.4 | 0.66 | 0.02 | 0.08 | 0.00 | 7.27 | 0.20 | 497 | ± | 8 |
| RL-6@8 | 32.3 | 0.7 | 23.9 | 0.5 | 0.68 | 0.02 | 0.09 | 0.00 | 8.15 | 0.16 | 538 | ± | 10 |
| RL-6@9 | 35.4 | 0.3 | 19.5 | 0.3 | 0.65 | 0.02 | 0.09 | 0.00 | 7.72 | 0.13 | 526 | ± | 10 |
| RL-6@10 | 29.8 | 0.3 | 9.7 | 0.3 | 0.67 | 0.02 | 0.09 | 0.00 | 8.29 | 0.22 | 540 | ± | 9 |
| RL-6@11 | 47.1 | 0.5 | 24.6 | 0.4 | 0.61 | 0.01 | 0.07 | 0.00 | 5.55 | 0.10 | 412 | ± | 5 |
| RL-6@12 | 36.5 | 0.4 | 16.8 | 0.3 | 0.63 | 0.02 | 0.08 | 0.00 | 7.09 | 0.14 | 504 | ± | 6 |
| RL-6@13 | 34.9 | 0.4 | 13.8 | 0.2 | 0.68 | 0.02 | 0.08 | 0.00 | 7.73 | 0.17 | 513 | ± | 8 |
| RL-6@14 | 39.9 | 0.4 | 18.6 | 0.4 | 0.62 | 0.02 | 0.08 | 0.00 | 6.51 | 0.15 | 472 | ± | 8 |
| RL-6@15 | 21.5 | 0.3 | 7.5 | 0.2 | 0.73 | 0.02 | 0.12 | 0.00 | 12.51 | 0.30 | 758 | ± | 12 |
| RL-6@16 | 39.5 | 0.6 | 36.6 | 1.2 | 0.62 | 0.02 | 0.07 | 0.00 | 5.93 | 0.17 | 434 | ± | 12 |
| RL-6@17 | 33.7 | 0.5 | 13.6 | 0.3 | 0.67 | 0.02 | 0.08 | 0.00 | 7.80 | 0.16 | 523 | ± | 6 |
| RL-6@18 | 22.2 | 0.3 | 26.7 | 0.5 | 0.73 | 0.01 | 0.14 | 0.00 | 13.97 | 0.23 | 838 | ± | 12 |
| RL-6@19 | 53.1 | 0.7 | 42.1 | 0.7 | 0.60 | 0.02 | 0.07 | 0.00 | 5.38 | 0.14 | 408 | ± | 7 |
| RL-6@20 | 34.5 | 0.4 | 12.5 | 0.4 | 0.64 | 0.01 | 0.08 | 0.00 | 7.08 | 0.13 | 494 | ± | 8 |
| RL-6@21 | 29.8 | 0.2 | 11.7 | 0.3 | 0.68 | 0.02 | 0.09 | 0.00 | 8.39 | 0.20 | 558 | ± | 9 |
| RL-6@22 | 38.8 | 0.4 | 18.2 | 0.3 | 0.64 | 0.02 | 0.08 | 0.00 | 6.81 | 0.10 | 473 | ± | 6 |
| RL-6@23 | 27.4 | 0.2 | 10.2 | 0.2 | 0.68 | 0.02 | 0.10 | 0.00 | 9.06 | 0.21 | 592 | ± | 13 |
| RL-6@24 | 45.1 | 1.2 | 44.7 | 2.0 | 0.62 | 0.02 | 0.07 | 0.00 | 5.94 | 0.20 | 430 | ± | 8 |
| RL-6@25 | 43.5 | 0.5 | 18.2 | 0.4 | 0.63 | 0.01 | 0.08 | 0.00 | 6.55 | 0.12 | 468 | ± | 6 |
| RL-6@26 | 51.7 | 0.7 | 41.0 | 1.5 | 0.60 | 0.03 | 0.07 | 0.00 | 5.54 | 0.17 | 415 | ± | 12 |
| RL-6@27 | 52.1 | 0.4 | 43.0 | 0.7 | 0.58 | 0.02 | 0.06 | 0.00 | 5.02 | 0.15 | 381 | ± | 8 |
| RL-6@28 | 51.9 | 0.5 | 43.7 | 0.5 | 0.59 | 0.01 | 0.06 | 0.00 | 5.23 | 0.09 | 403 | ± | 6 |
| RL-6@29 | 39.7 | 0.4 | 17.8 | 0.4 | 0.62 | 0.01 | 0.07 | 0.00 | 6.08 | 0.13 | 446 | ± | 7 |

| | | | | | | | | | | | | | |
|---|---|---|---|---|---|---|---|---|---|---|---|---|---|
| RL-6@30 | 29.0 | 0.3 | 12.0 | 0.3 | 0.67 | 0.01 | 0.09 | 0.00 | 8.77 | 0.17 | 581 | ± | 11 |
| RL-6@31 | 14.9 | 0.7 | 5.3 | 0.3 | 0.75 | 0.02 | 0.16 | 0.01 | 16.43 | 0.72 | 957 | ± | 34 |
| RL-6@32 | 38.4 | 0.5 | 17.0 | 0.3 | 0.65 | 0.02 | 0.08 | 0.00 | 7.13 | 0.14 | 492 | ± | 7 |
| RL-6@33 | 39.8 | 0.4 | 22.0 | 0.4 | 0.63 | 0.02 | 0.08 | 0.00 | 6.63 | 0.14 | 472 | ± | 7 |
| RL-6@34 | 39.0 | 0.5 | 16.6 | 0.3 | 0.64 | 0.02 | 0.08 | 0.00 | 7.08 | 0.15 | 506 | ± | 8 |
| RL-6@35 | 31.5 | 0.2 | 10.8 | 0.3 | 0.65 | 0.02 | 0.09 | 0.00 | 8.05 | 0.17 | 555 | ± | 8 |
| RL-6@36 | 71.7 | 1.0 | 70.2 | 3.0 | 0.49 | 0.02 | 0.05 | 0.00 | 3.17 | 0.10 | 290 | ± | 5 |
| RL-6@37 | 32.6 | 0.3 | 13.3 | 0.3 | 0.66 | 0.02 | 0.09 | 0.00 | 7.81 | 0.18 | 530 | ± | 7 |
| RL-6@38 | 34.1 | 0.2 | 13.8 | 0.2 | 0.65 | 0.02 | 0.08 | 0.00 | 7.48 | 0.16 | 518 | ± | 9 |
| RL-6@39 | 32.5 | 0.4 | 12.8 | 0.3 | 0.65 | 0.01 | 0.08 | 0.00 | 7.51 | 0.15 | 510 | ± | 8 |
| RL-6@40 | 34.9 | 0.5 | 14.7 | 0.3 | 0.65 | 0.02 | 0.08 | 0.00 | 7.08 | 0.13 | 492 | ± | 7 |
| RL-6@41 | 41.8 | 0.2 | 21.2 | 0.5 | 0.63 | 0.02 | 0.07 | 0.00 | 6.26 | 0.13 | 451 | ± | 8 |
| RL-6@42 | 30.9 | 0.7 | 11.5 | 0.3 | 0.67 | 0.02 | 0.09 | 0.00 | 8.56 | 0.21 | 570 | ± | 12 |
| RL-6@43 | 28.3 | 0.2 | 12.8 | 0.3 | 0.69 | 0.01 | 0.09 | 0.00 | 9.01 | 0.17 | 579 | ± | 12 |
| RL-6@44 | 28.8 | 1.2 | 13.3 | 0.4 | 0.69 | 0.02 | 0.10 | 0.00 | 9.43 | 0.37 | 603 | ± | 17 |
| RL-6@45 | 27.5 | 0.6 | 14.4 | 0.5 | 0.70 | 0.02 | 0.09 | 0.00 | 9.03 | 0.26 | 581 | ± | 13 |
| RL-10 | | | | | | | | | | | | | |
| RL-10@1 | 19.2 | 0.1 | 7.6 | 0.2 | 0.74 | 0.02 | 0.15 | 0.00 | 15.54 | 0.43 | 915 | ± | 16 |
| RL-10@2 | 22.2 | 0.2 | 7.7 | 0.2 | 0.71 | 0.02 | 0.14 | 0.00 | 13.19 | 0.25 | 818 | ± | 16 |
| RL-10@3 | 26.2 | 0.2 | 7.7 | 0.3 | 0.72 | 0.02 | 0.12 | 0.00 | 12.17 | 0.33 | 739 | ± | 15 |
| RL-10@4 | 16.5 | 0.1 | 8.6 | 0.3 | 0.76 | 0.02 | 0.17 | 0.00 | 17.20 | 0.38 | 985 | ± | 18 |
| RL-10@5 | 16.1 | 0.4 | 8.9 | 0.2 | 0.73 | 0.02 | 0.16 | 0.00 | 16.60 | 0.35 | 965 | ± | 22 |
| RL-10@6 | 10.7 | 0.1 | 5.8 | 0.2 | 0.79 | 0.02 | 0.24 | 0.00 | 25.88 | 0.57 | 1372 | ± | 25 |
| RL-10@7 | 20.5 | 0.3 | 10.0 | 0.6 | 0.73 | 0.02 | 0.14 | 0.00 | 13.98 | 0.32 | 834 | ± | 14 |
| RL-10@8 | 11.5 | 0.2 | 10.0 | 0.3 | 0.80 | 0.02 | 0.22 | 0.00 | 23.33 | 0.66 | 1257 | ± | 21 |
| RL-10@9 | 13.2 | 0.3 | 5.2 | 0.2 | 0.79 | 0.02 | 0.19 | 0.00 | 20.32 | 0.43 | 1119 | ± | 22 |
| RL-10@10 | 6.7 | 0.1 | 6.1 | 0.2 | 0.81 | 0.02 | 0.30 | 0.01 | 33.70 | 0.74 | 1704 | ± | 28 |
| RL-10@11 | 18.7 | 0.1 | 6.6 | 0.3 | 0.74 | 0.02 | 0.13 | 0.00 | 12.84 | 0.35 | 767 | ± | 19 |
| RL-10@12 | 14.3 | 0.5 | 5.5 | 0.3 | 0.76 | 0.02 | 0.15 | 0.00 | 15.46 | 0.53 | 892 | ± | 24 |
| RL-10@13 | 12.7 | 0.1 | 5.0 | 0.2 | 0.78 | 0.02 | 0.22 | 0.00 | 23.62 | 0.43 | 1285 | ± | 22 |
| RL-10@14 | 10.1 | 0.1 | 3.5 | 0.1 | 0.77 | 0.02 | 0.26 | 0.01 | 27.46 | 0.51 | 1482 | ± | 28 |
| RL-10@15 | 16.2 | 0.2 | 6.6 | 0.2 | 0.75 | 0.02 | 0.16 | 0.00 | 16.46 | 0.38 | 956 | ± | 16 |
| RL-10@16 | 14.9 | 0.2 | 6.3 | 0.2 | 0.75 | 0.02 | 0.16 | 0.00 | 16.63 | 0.50 | 965 | ± | 21 |

| | | | | | | | | | | | | | |
|---|---|---|---|---|---|---|---|---|---|---|---|---|---|
| RL-10@17 | 9.9 | 0.1 | 8.8 | 0.3 | 0.81 | 0.02 | 0.23 | 0.00 | 25.87 | 0.63 | 1356 | ± | 20 |
| RL-10@18 | 14.5 | 0.2 | 8.2 | 0.2 | 0.77 | 0.02 | 0.19 | 0.00 | 19.83 | 0.45 | 1106 | ± | 20 |
| RL-10@19 | 7.2 | 0.1 | 8.0 | 0.2 | 0.81 | 0.02 | 0.33 | 0.01 | 37.90 | 0.74 | 1847 | ± | 28 |
| RL-10@20 | 16.1 | 0.3 | 10.5 | 0.3 | 0.77 | 0.02 | 0.17 | 0.00 | 18.15 | 0.45 | 1018 | ± | 16 |
| RL-10@21 | 8.5 | 0.1 | 5.3 | 0.1 | 0.78 | 0.02 | 0.25 | 0.00 | 26.69 | 0.57 | 1432 | ± | 23 |
| RL-10@22 | 17.2 | 0.3 | 9.3 | 0.3 | 0.76 | 0.02 | 0.16 | 0.00 | 15.98 | 0.32 | 937 | ± | 16 |
| RL-10@23 | 13.0 | 0.3 | 7.6 | 0.2 | 0.75 | 0.02 | 0.18 | 0.00 | 18.62 | 0.38 | 1068 | ± | 22 |
| RL-10@24 | 9.6 | 0.1 | 5.6 | 0.1 | 0.78 | 0.02 | 0.23 | 0.00 | 25.17 | 0.54 | 1333 | ± | 23 |
| RL-10@25 | 20.6 | 0.2 | 7.9 | 0.2 | 0.74 | 0.02 | 0.13 | 0.00 | 13.13 | 0.26 | 777 | ± | 11 |
| RL-16 | | | | | | | | | | | | | |
| RL-16@1 | 22.7 | 0.3 | 26.9 | 0.4 | 0.74 | 0.02 | 0.14 | 0.00 | 14.25 | 0.27 | 848 | ± | 15 |
| RL-16@2 | 23.4 | 0.2 | 28.3 | 0.4 | 0.75 | 0.01 | 0.14 | 0.00 | 14.38 | 0.23 | 836 | ± | 10 |
| RL-16@3 | 28.6 | 0.3 | 29.7 | 0.6 | 0.74 | 0.01 | 0.14 | 0.00 | 13.93 | 0.26 | 823 | ± | 14 |
| RL-16@4 | 21.9 | 0.2 | 24.2 | 0.4 | 0.77 | 0.01 | 0.15 | 0.00 | 16.46 | 0.27 | 916 | ± | 14 |
| RL-16@5 | 16.7 | 0.6 | 17.6 | 0.6 | 0.77 | 0.02 | 0.19 | 0.01 | 20.22 | 0.60 | 1123 | ± | 35 |
| RL-16@6 | 21.2 | 0.2 | 25.4 | 0.4 | 0.74 | 0.02 | 0.14 | 0.00 | 14.39 | 0.30 | 841 | ± | 10 |
| RL-16@7 | 20.0 | 0.3 | 24.5 | 0.4 | 0.78 | 0.02 | 0.17 | 0.00 | 17.77 | 0.37 | 1003 | ± | 19 |
| RL-16@8 | 22.1 | 0.2 | 28.6 | 0.4 | 0.77 | 0.02 | 0.15 | 0.00 | 15.52 | 0.26 | 893 | ± | 14 |
| RL-16@9 | 22.5 | 0.2 | 26.7 | 0.3 | 0.75 | 0.01 | 0.16 | 0.00 | 16.88 | 0.28 | 972 | ± | 14 |
| RL-16@10 | 55.2 | 1.2 | 199.5 | 5.6 | 0.66 | 0.01 | 0.09 | 0.00 | 7.93 | 0.20 | 541 | ± | 11 |
| RL-16@11 | 13.1 | 0.8 | 20.7 | 0.8 | 0.82 | 0.02 | 0.29 | 0.02 | 32.40 | 2.00 | 1634 | ± | 82 |
| RL-16@12 | 15.7 | 0.1 | 12.8 | 0.3 | 0.78 | 0.02 | 0.18 | 0.00 | 19.87 | 0.35 | 1093 | ± | 16 |
| RL-16@13 | 19.7 | 0.3 | 23.2 | 0.5 | 0.77 | 0.03 | 0.19 | 0.01 | 20.25 | 1.29 | 1107 | ± | 41 |
| RL-16@14 | 19.7 | 0.2 | 24.2 | 0.4 | 0.74 | 0.02 | 0.15 | 0.00 | 15.18 | 0.33 | 900 | ± | 10 |
| RL-16@15 | 20.1 | 0.2 | 22.3 | 0.3 | 0.75 | 0.01 | 0.18 | 0.00 | 18.46 | 0.33 | 1049 | ± | 15 |
| RL-16@16 | 17.7 | 0.2 | 17.7 | 0.4 | 0.77 | 0.01 | 0.19 | 0.00 | 20.38 | 0.36 | 1133 | ± | 16 |
| RL-16@17 | 15.9 | 0.3 | 13.7 | 0.3 | 0.79 | 0.02 | 0.20 | 0.00 | 21.67 | 0.54 | 1156 | ± | 23 |
| RL-16@18 | 23.7 | 0.3 | 30.5 | 0.5 | 0.74 | 0.02 | 0.15 | 0.00 | 14.96 | 0.22 | 896 | ± | 14 |
| RL-16@19 | 17.0 | 0.1 | 15.5 | 0.3 | 0.77 | 0.02 | 0.18 | 0.00 | 19.22 | 0.37 | 1071 | ± | 16 |
| RL-16@20 | 29.8 | 4.1 | 13.0 | 1.6 | 0.70 | 0.03 | 0.11 | 0.01 | 11.23 | 1.62 | 681 | ± | 73 |
| RL-16@21 | 38.1 | 4.6 | 22.0 | 2.5 | 0.67 | 0.04 | 0.09 | 0.01 | 8.30 | 1.03 | 552 | ± | 57 |
| RL-16@22 | 15.8 | 0.3 | 18.3 | 0.5 | 0.78 | 0.03 | 0.20 | 0.01 | 20.93 | 0.54 | 1149 | ± | 29 |
| RL-16@23 | 21.4 | 0.2 | 55.8 | 0.9 | 0.76 | 0.02 | 0.16 | 0.00 | 17.09 | 0.44 | 970 | ± | 18 |

| | | | | | | | | | | | | | |
|---|---|---|---|---|---|---|---|---|---|---|---|---|---|
| RL-16@24 | 15.2 | 0.1 | 26.0 | 0.3 | 0.77 | 0.02 | 0.23 | 0.00 | 24.47 | 0.39 | 1344 | ± | 18 |
| RL-16@25 | 20.8 | 1.4 | 21.1 | 1.1 | 0.76 | 0.02 | 0.17 | 0.01 | 17.46 | 1.21 | 1007 | ± | 64 |
| RL-16@26 | 19.1 | 0.1 | 23.9 | 0.4 | 0.76 | 0.02 | 0.15 | 0.00 | 16.23 | 0.30 | 916 | ± | 13 |
| RL-16@27 | 20.1 | 0.1 | 25.0 | 0.4 | 0.74 | 0.02 | 0.15 | 0.00 | 14.93 | 0.29 | 885 | ± | 12 |
| RL-16@28 | 22.3 | 0.2 | 25.3 | 0.4 | 0.75 | 0.02 | 0.15 | 0.00 | 15.91 | 0.31 | 922 | ± | 15 |
| RL-16@29 | 17.1 | 0.2 | 16.1 | 0.3 | 0.78 | 0.01 | 0.19 | 0.00 | 20.27 | 0.36 | 1113 | ± | 16 |
| RL-16@30 | 22.1 | 0.3 | 28.2 | 0.3 | 0.76 | 0.02 | 0.14 | 0.00 | 15.07 | 0.29 | 872 | ± | 14 |
| RL-16@31 | 22.2 | 0.2 | 26.9 | 0.5 | 0.72 | 0.02 | 0.14 | 0.00 | 14.05 | 0.21 | 841 | ± | 16 |
| RL-16@32 | 19.8 | 0.3 | 22.4 | 0.4 | 0.76 | 0.01 | 0.18 | 0.00 | 18.55 | 0.34 | 1069 | ± | 16 |
| RL-16@33 | 29.3 | 0.3 | 52.8 | 0.7 | 0.73 | 0.02 | 0.12 | 0.00 | 12.52 | 0.22 | 749 | ± | 11 |
| RL-16@34 | 27.8 | 0.3 | 47.3 | 0.6 | 0.74 | 0.01 | 0.13 | 0.00 | 13.08 | 0.22 | 775 | ± | 10 |
| RL-16@35 | 17.6 | 0.2 | 22.1 | 0.5 | 0.74 | 0.02 | 0.17 | 0.00 | 17.36 | 0.44 | 1002 | ± | 20 |
| RL-16@36 | 29.5 | 0.2 | 119.2 | 1.1 | 0.72 | 0.02 | 0.13 | 0.00 | 13.13 | 0.24 | 790 | ± | 13 |
| RL-16@37 | 24.6 | 0.9 | 25.8 | 0.7 | 0.73 | 0.02 | 0.13 | 0.00 | 13.47 | 0.54 | 803 | ± | 24 |
| RL-16@38 | 29.0 | 0.6 | 25.6 | 0.6 | 0.73 | 0.02 | 0.12 | 0.00 | 12.66 | 0.30 | 757 | ± | 16 |
| RL-16@39 | 17.9 | 0.2 | 18.4 | 0.3 | 0.77 | 0.01 | 0.19 | 0.00 | 20.25 | 0.35 | 1118 | ± | 19 |
| RL-16@40 | 21.7 | 0.2 | 25.8 | 0.4 | 0.76 | 0.02 | 0.16 | 0.00 | 16.48 | 0.30 | 949 | ± | 14 |

## 5. Discussion

### *5.1. Origin of the Apatite from the Renli Deposit*

Many studies have considered that the apatite includes magmatic (mixing, inheritance, and composition variation of the host magma) and hydrothermal apatite [38–42]. Among these, magma mixing and inheritance can lead to sudden changes in the composition of apatite, but the REE in apatite is not easily redistributed [4,43]. RL-6, RL-10, and RL-16 apatite show similar chondrite-normalized REE patterns and a gradual decrease in ΣREE. Therefore, magma mixing and inheritance are unlikely.

The levels of LOI of RL-6, RL-10, and RL-16 are less than 1 wt.%, and they do not have porosity, which indicates that post-magmatic alteration or weathering is not obvious [44]. The unsaturated fluid of REE infiltrates through apatite, and monazite inclusions will be formed in apatite [45,46]. Monazite will extract LREE from the more fractionated melts, resulting in the depletion of these elements in apatite [47]. The contents of LREE in RL-6, RL-10, and RL-16 are enriched, and the LREE/HREE ranges from 3.61 to 24.07 (Figure 8i). Therefore, hydrothermal alteration is unlikely. Moreover, the apatites have a subhedral to anhedral structure and the surface of backscattered electron (BSE) images are homogeneous without fractures (Figure 4g–i). The chondrite-normalized REE patterns of RL-6, RL-10, and RL-16 apatite vary systematically and are similar to those of pegmatite in the Renli deposit (Figures 7), suggesting that is the result of gradually magmatic evolution. Cl in apatite will preferentially combine with LREE, resulting in the separation of LREE and HREE [48,49]. However, the separation degree of LREE and HREE is low, especially in the RL-6 and RL-10 samples (Figure 8). In brief, according to apatite texture and composition of apatite, we confirm that the origin of the RL-6, RL-10, and RL-16 apatite is magmatic.

### *5.2. Time of Nb-Ta Mineralization and Tectonic Environment*

Many studies have been conducted on the geochronology of the Renli Nb-Ta deposit. The Zircon U-Pb age obtained by Xiong et al. (2020) from biotite monzogranite was 154 ± 3 Ma, and this represents the crystallization age of biotite monzogranite in the Renli Nb-Ta deposit [14]. The zircon U-Pb age obtained by Xiong et al. (2020) from muscovite monzogranite was 141 ± 2 Ma, and a SHRIMP Zircon U-Pb age obtained by Li et al. (2017) was ca. 137 Ma [13]. Regarding the time of mineralization, a muscovite $^{40}Ar$–$^{39}Ar$ age range obtained by Li et al. (2017) for the Mufushan complex granite ore-bearing pegmatite was 131–128 Ma, and a coltan U-Pb age obtained by Xiong et al. (2020) was ~140 Ma [13,14]. Because of extensive mineralization, many studies confirm that biotite monzogranite and muscovite monzogranite from the Mufushan granite are spatially and genetically related to the Renli Nb-Ta deposit [14]. The new LA-ICP-MS apatite U-Pb ages obtained from the two-mica pegmatite were approximately 130 Ma, which is consistent with the muscovite $^{40}Ar$–$^{39}Ar$ age reported by Li et al. (2017) [13]. South China was in a lithospheric extension system during the period around 140 Ma [50–52]. Therefore, the Renli deposit likely formed in an extensional environment, and the Nb-Ta mineralization of Renli deposit lasted until approximately 130 Ma.

The apatite U-Pb system is characterized by a relatively low closure temperature ranging from 350 to 550 °C, so the system can be easily reset during heating [3]. For the RL-6, RL-10, and RL-16 samples, the LA-ICP-MS U-Pb ages of apatite are almost the same (within the uncertainty range), and the mean value is approximately 130 Ma. The LA-ICP-MS U-Pb age of zircon from the columbite-bearing albite pegmatite is 131 ± 2 Ma, which represents the age of new magmatic–hydrothermal growth and recrystallization in the giant Renli Nb-Ta deposit [19]. The youngest LA-ICP-MS U-Pb age of zircon from columbite-bearing albite pegmatite and the apatite U-Pb age under LA-ICP-MS are similar. Therefore, one possible explanation is that the U-Pb system in apatite crystals is subsequently disturbed throughout the block, which is the result of the inflow of the youngest mantle-related granitic magma and the growth and recrystallization of the new

magmatic–hydrothermal solution [3]. This suggests that there was no younger thermal event (above 350 °C) in the Renli area [3].

*5.3. Oxidation State of Nb-Ta Mineralization*

Apatite is an important accessory mineral in various magmatic rocks, and $Ca^{2+}$ can be occupied by a number of cations, such as $Na^{+}$, $Fe^{2+}$, $Mn^{2+}$, $Sr^{2+}$, rare earth elements ($REE^{2+/3+}$), and $Y^{3+}$ [4,53–56]. The trace elements in apatite depend on the characteristics of the host rock, so the geochemical characteristics of apatite can be used to interpret the mineralogical and geological conditions [57–63]. Large quantities of elements (Ce, Eu, and Mn) enter apatite, and due to the variable oxidation of these elements, their anomalies in apatite can be used to indicate the redox state of magma [47,64,65].

In this study, the RL-6, RL-10, and RL-16 samples do not have significant Ce anomalies; the Ce anomalies range from 1.02 to 1.22. All the analyzed apatite has strong negative Eu anomalies (Figure 7). Eu anomalies are strongly controlled by feldspar crystallization prior to or simultaneously with apatite crystallization, so it is difficult to explain the oxidation state of the host felsic magma [47,66,67]. The Sr content of apatite has nothing to do with oxidation state [68]. The Sr content of pegmatite is lower than the Sr content of apatite, which also supports the plagioclase crystallization. Previous studies have used Mn anomalies to indicate the redox state of magma, because the radius of $Mn^{2+}$ is more similar to that of $Ca^{2+}$; reduced magmas have a higher content of Mn than oxidized magma [47]. Because the Mn contents of the whole rock are >100 ppm, this effect will be obscured during the fractionation of granitoid magmas [47]. In contrast to Mn, the content of Ga in apatite is independent of the host rock; because the radius of $Ga^{2+}$ is more similar to that of $Ca^{2+}$, reduced magmas a have higher content of Ga than oxidized magmas [69]. We found that the Ga content decreases successively from the RL-6 and RL-10 rock to the RL-16 rock, so the degree of oxidation gradually increases. In addition, compared with rocks with a lower oxidation degree, apatite in the rocks with a higher oxidation degree has a lower Y/ΣREE ratio, a higher La/Sm ratio, and a higher Ce/Th ratio [47]. The Y/ΣREE ratio ranges from 0.44 to 0.69 in RL-6 apatite and ranges from 0.05 to 0.46 in RL-16 apatite (Figure 8d). The gradual reduction in the Y/ΣREE ratio in apatite from the Renli pegmatites indicates an increase in the oxidation degree of the Nb-Ta mineralization in the giant Renli deposit. Compare to pegmatite, the apatite has higher content of Y and HREE, suggesting that the apatite is product of water-poor melts [68]. Highly evolved and volatile rich magmas have a non-chondrite Y/Ho ratio [25]. The mostly Y/Ho ratio of RL-6, RL-10, and RL-16 are >34, which indicate that its host pegmatite is formed in a transitional magmatic-hydrothermal system [1]. In brief, the REE behavior of apatite can be used to constrain the oxidation state of Nb-Ta mineralization, and apatite has great potential as an exploration indicator.

## 6. Conclusions

(1) The origin of the apatite is magmatic, and the oxidation degree of the Nb-Ta mineralization increases in the giant Renli deposit.
(2) The Renli Nb-Ta deposit likely formed in an extensional environment, the Nb-Ta mineralization lasted until approximately 130 Ma, and there was no younger thermal event (above 350 °C) in the Renli deposit.
(3) The host pegmatite of apatite from Renli deposit is formed in a transitional magmatic-hydrothermal system. The combination of the composition and U-Pb ages of apatite can be used to constrain the magmatic–hydrothermal evolution of granite and pegmatite-type Nb-Ta deposits.

**Author Contributions:** Conceptualization, Y.C. and Z.X.; methodology, Y.C., Z.X., and H.D.; formal analysis, Z.X. and H.D.; investigation, Y.C., Z.X., Z.Z., C.M., F.Z., L.Z., and J.C.; resources, H.T., J.H., F.Z., L.Z., J.C., and C.W.; writing—original draft preparation, Y.C., Z.X., and H.D. All authors have read and agreed to the published version of the manuscript.

**Funding:** This research was funded by The National Natural Science Foundation of China Project (42130810), National Key Research and Development Program of Hunan Province (2019SK2261), The Science and Technology Innovation Leading Talent Project of Hunan Province (2020RC4003), The Scientific and Technological Talents Support Engineering Project of Hunan Province (202TJ-Q01), and The Science and Technology Innovation Program of Hunan Province (2021RC4055).

**Conflicts of Interest:** The authors declare no conflict of interest.

## References

1. Jiang, S.Y.; Wen, H.J.; Xu, C.; Wang, Y.; Sun, W.D. Earth sphere cycling and enrichment mechanism of critical metals: Major scientific issues for future research. *Bull. Natl. Nat. Sci. Found. China* **2019**, *33*, 112–118, https://doi.org/10.16262/j.cnki.1000–8217.2019.02.003. (In Chinese with English abstract)
2. Wang, R.; Che, X.; Wu, B.; Xie, L. Critical mineral resources of Nb, Ta, Zr, and Hf in China. *Chin. Sci. Bull.* **2020**, *65*, 3763–3777, https://doi.org/10.1360/tb-2020-0271. (In Chinese with English abstract)
3. Gawęda, A.; Szopa, K.; Chew, D. LA-ICP-MS U-Pb dating and REE patterns of apatite from the Tatra Mountains, Poland as a monitor of the regional tectonomagmatic activity. *Geochronometria* **2014**, *41*, 306–314, https://doi.org/10.2478/s13386-013-0171-0.
4. Zhang, W.; Jiang, S.-Y.; Ouyang, Y.; Zhang, D. Geochronology and textural and compositional complexity of apatite from the mineralization-related granites in the world-class Zhuxi W-Cu skarn deposit: A record of magma evolution and W enrichment in the magmatic system. *Ore Geol. Rev.* **2021**, *128*, 103885, https://doi.org/10.1016/j.oregeorev.2020.103885.
5. Toplis, M.; Dingwell, D. The variable influence of P2O5 on the viscosity of melts of differing alkali/aluminium ratio: Implications for the structural role of phosphorus in silicate melts. *Geochim. Cosmochim. Acta* **1996**, *60*, 4107–4121, https://doi.org/10.1016/s0016-7037(96)00225-6.
6. Pan, Y.; Fleet, M.E. Compositions of the Apatite-Group Minerals: Substitution Mechanisms and Controlling Factors. *Rev. Miner. Geochem.* **2002**, *48*, 13–49, https://doi.org/10.2138/rmg.2002.48.2.
7. Cao, M.J.; Evans, N.J.; Hollings, P.; Cooke, D.R.; McInnes, B.I.; Qin, K. Apatite Texture, Composition, and O-Sr-Nd Isotope Signatures Record Magmatic and Hydrothermal Fluid Characteristics at the Black Mountain Porphyry Deposit, Philippines. *Econ. Geol.* **2021**, *116*, 1189–1207, https://doi.org/10.5382/econgeo.4827.
8. Amelin, Y.; Zaitsev, A. Precise geochronology of phoscorites and carbonatites: The critical role of U-series disequilibrium in age interpretations. *Geochim. Cosmochim. Acta* **2002**, *66*, 2399–2419, https://doi.org/10.1016/s0016-7037(02)00831-1.
9. Gleadow, A.J.; Belton, D.X.; Kohn, B.P.; Brown, R.W. Fission Track Dating of Phosphate Minerals and the Thermochronology of Apatite. *Rev. Miner. Geochem.* **2002**, *48*, 579–630, https://doi.org/10.2138/rmg.2002.48.16.
10. Cherniak, D. Uranium and manganese diffusion in apatite. *Chem. Geol.* **2005**, *219*, 297–308, https://doi.org/10.1016/j.chemgeo.2005.02.014.
11. Li, Q.; Li, X.-H.; Wu, F.-Y.; Yin, Q.-Z.; Ye, H.-M.; Liu, Y.; Tang, G.-Q.; Zhang, C.-L. In-situ SIMS U–Pb dating of phanerozoic apatite with low U and high common Pb. *Gondwana Res.* **2012**, *21*, 745–756, https://doi.org/10.1016/j.gr.2011.07.008.
12. Chew, D.M.; Babechuk, M.G.; Cogné, N.; Mark, C.; O'Sullivan, G.; Henrichs, I.A.; Doepke, D.; McKenna, C.A. (LA,Q)-ICPMS trace-element analyses of Durango and McClure Mountain apatite and implications for making natural LA-ICPMS mineral standards. *Chem. Geol.* **2016**, *435*, 35–48, https://doi.org/10.1016/j.chemgeo.2016.03.028.
13. Li, P. *Magmatic Activities and Metallogenic Regularity of Rare Metals of Mufushan Area*; (Post-Doctoral Outbound Report); Institute of Mineral Resources, Chinese Academy of Geological Sciences: Beijing, China, 2017; p. 301. (In Chinese with English abstract)
14. Xiong, Y.-Q.; Jiang, S.-Y.; Wen, C.-H.; Yu, H.-Y. Granite–pegmatite connection and mineralization age of the giant Renli Ta Nb deposit in South China: Constraints from U–Th–Pb geochronology of coltan, monazite, and zircon. *Lithos* **2020**, *358–359*, 105422, https://doi.org/10.1016/j.lithos.2020.105422.
15. Li, P.; Li, J.; Chen, Z.; Liu, X.; Huang, Z.; Zhou, F. Compositional evolution of the muscovite of Renli pegmatite-type rare-metal deposit, northeast Hunan, China: Implications for its petrogenesis and mineralization potential. *Ore Geol. Rev.* **2021**, *138*, 104380, https://doi.org/10.1016/j.oregeorev.2021.104380.
16. Wang, X.-L.; Zhou, J.-C.; Griffin, W.L.; Wang, R.-C.; Qiu, J.-S.; O'Reilly, S.Y.; Xu, X.; Liu, X.-M.; Zhang, G.-L. Detrital zircon geochronology of Precambrian basement sequences in the Jiangnan orogen: Dating the assembly of the Yangtze and Cathaysia Blocks. *Precambrian Res.* **2007**, *159*, 117–131, https://doi.org/10.1016/j.precamres.2007.06.005.
17. Zheng, Y.-F.; Xiao, W.-J.; Zhao, G. Introduction to tectonics of China. *Gondwana Res.* **2013**, *23*, 1189–1206, https://doi.org/10.1016/j.gr.2012.10.001.
18. Zhao, G. Jiangnan Orogen in South China: Developing from divergent double subduction. *Gondwana Res.* **2015**, *27*, 1173–1180, https://doi.org/10.1016/j.gr.2014.09.004.
19. Li, P.; Li, J.; Liu, X.; Li, C.; Huang, Z.; Zhou, F. Geochronology and source of the rare-metal pegmatite in the Mufushan area of the Jiangnan orogenic belt: A case study of the giant Renli Nb–Ta deposit in Hunan, China. *Ore Geol. Rev.* **2020**, *116*, 103237, https://doi.org/10.1016/j.oregeorev.2019.103237.
20. Liu, X.; Zhou, F.C.; Huang, Z.B.; Li, J.K.; Zhou, H.X.; Xiao, G.Q.; Bao, Y.H.; Li, P.; Tan, L.M.; Shi, W.K.; et al. Discovery of Renli Superlarge Pegmatite-type Nb-Ta Polymetallic Deposit in Pingjiang, Hunan Province and its Significances. *Geotecton. Metallog.* **2018**, *42*, 235–243, https://doi.org/10.16539/j.ddgzyckx.2018.02.004. (In Chinese with English abstract)

21. Xu, D.R.; Deng, T.; Dong, G.J.; Ning, J.T.; Wang, Z.L.; Zhang, J.L.; Zou, F.H.; Zhou, Y.Q.; Chen, G.W.; Yu, D.S.; et al. Zircon U-Pb geochronological and geochemical characteristics of the Lianyunshan two-mica monzogranites in northeastern Hunan province: Implications for petrogenesis and tectonic setting associated with polymetallic mineralization. *Earth Sci. Front.* **2017**, *24*, 104–122, https://doi.org/10.13745/j.esf.2017.02.011. (In Chinese with English abstract)
22. Zhou, F.C.; Li, J.K.; Liu, X.; Li, P.; Huang, Z.B.; Shi, W.K.; Su, J.N.; Chen, H.; Huang, X.Q. Geochemical Characteristics and genetic significance of ore bodies in RenLi Nb-Ta deposit, Hunan province. *Acta Geol. Sin.* **2019**, *93*, 1392–1404, https://doi.org/10.19762/j.cnki.dizhixuebao.2019144. (In Chinese with English abstract)
23. Che, X.-D.; Wang, R.-C.; Wu, F.-Y.; Zhu, Z.-Y.; Zhang, W.-L.; Hu, H.; Xie, L.; Lu, J.-J.; Zhang, D. Episodic Nb–Ta mineralisation in South China: Constraints from in situ LA–ICP–MS columbite-tantalite U–Pb dating. *Ore Geol. Rev.* **2019**, *105*, 71–85, https://doi.org/10.1016/j.oregeorev.2018.11.023.
24. Shu, L.S.; Jahn, B.-M.; Charvet, J.; Santosh, M.; Wang, B.; Xu, X.S.; Jiang, S.Y. Early Paleozoic depositional environment and intraplate tectono-magmatism in the Cathaysia Block (South China): Evidence from stratigraphic, structural, geochemical and geochronological investigations. *Am. J. Sci.* **2014**, *314*, 154–186, https://doi.org/10.2475/01.2014.05.
25. Xiong, Y.-Q.; Shao, Y.-J.; Cheng, Y.; Jiang, S.-Y. Discrete Jurassic and Cretaceous Mineralization Events at the Xiangdong W(-Sn) Deposit, Nanling Range, South China. *Econ. Geol.* **2020**, *115*, 385–413, https://doi.org/10.5382/econgeo.4704.
26. Xiong, Y.Q.; Shao, Y.J.; Mao, J.W.; Wu, S.C.; Zhou, H.D.; Zheng, M.H. The polymetallic magmatic-hydrothermal Xiangdong and Dalong systems in the W-Sn-Cu-Pb-Zn-Ag Dengfuxian orefield, SE China: Constraints from geology, fluid inclusions, H-O-S-Pb isotopes, and sphalerite Rb-Sr geochronology. *Miner. Depos.* **2019**, *54*, 1101–1124.
27. Li, P.; Li, J.K.; Pei, R.F.; Leng, S.L.; Zhang, X.; Zhou, F.C.; Li, S.M. Multistage magmatic evolution and Cretaceous peak Metallogenic epochs of Mufushan composite granite mass: Constrains from Geochronological evidence. *Earth Sci.* **2017**, *42*, 1684–1696, https://doi.org/10.3799/dqkx.2017.114.
28. Li, C.Y. The Genesis of Chuanziyuan Niobium-Tantalum-Lithium Rare Metal Deposit in Pingjiang Hunan. Master's Thesis, Central South University, Changsha, China, 2016.
29. Wen, C.H.; Chen, J.F.; Luo, X.Y.; Li, S.M. Geochemical features of the Chuanziyuan rare metal pegmatite in northeastern Hunan, China. *Bull. Mineral. Petrol. Geochem.* **2016**, *35*, 171–177. (In Chinese with English abstract)
30. Wen, C.-H.; Shao, Y.-J.; Xiong, Y.-Q.; Li, J.-K.; Jiang, S.-Y. Ore genesis of the Baishawo Be-Li-Nb-Ta deposit in the northeast Hunan Province, south China: Evidence from geological, geochemical, and U-Pb and Re-Os geochronologic data. *Ore Geol. Rev.* **2021**, *129*, 103895, https://doi.org/10.1016/j.oregeorev.2020.103895.
31. Li, P.; Zhou, F.C.; Li, J.K.; Liu, X.; Huang, Z.B.; Zhang, L.P. Zircon U-Pb Ages and Hf Isotopic Compositions of the Concealed Granite of Renli-Chuanziyuan Deposit, NE Hunan and Geological Significance. *Geotecton. Metallog.* **2020**, *44*, 486–500, https://doi.org/10.16539/j.ddgzyckx.2020.03.012. (In Chinese with English abstract)
32. Zhou, F.C.; Liu, X.; Li, J.K.; Huang, Z.B.; Xiao, G.Q.; Li, P.; Zhou, H.X.; Shi, W.K.; Tan, L.M.; Su, J.N.; et al. Metallogenic characteristics and prospecting direction of Renli super-large rare metal deposit in Hunan province, China. *Geotecton. Metallog.* **2019**, *43*, 77–91, https://doi.org/10.16539/j.ddgzyckx.2019.01.007. (In Chinese with English abstract)
33. Thomson, S.N.; Gehrel, G.E.; Ruiz, J.; Buchwaldt, R. Routine low-damage apatite U-Pb dating using laser ablation-multicollector-ICP-MS. *Geochem. Geophys. Geosyst.* **2012**, *13*, Q0AA21.
34. Chew, D.; Petrus, J.; Kamber, B. U–Pb LA–ICPMS dating using accessory mineral standards with variable common Pb. *Chem. Geol.* **2014**, *363*, 185–199, https://doi.org/10.1016/j.chemgeo.2013.11.006.
35. Petrus, J.A.; Kamber, B. VizualAge: A Novel Approach to Laser Ablation ICP-MS U-Pb Geochronology Data Reduction. *Geostand. Geoanal. Res.* **2012**, *36*, 247–270, https://doi.org/10.1111/j.1751-908x.2012.00158.x.
36. Sun, S.S.; McDonough, W.F. *Chemical and Isotopic Systematics of Oceanic Basalts: Implications for Mantle Composition and Processes*; Geological Society of London Special Publication: London, UK, 1989; Volume 42, pp. 313–345.
37. Tera, F.; Wasserburg, G. U-Th-Pb systematics in three Apollo 14 basalts and the problem of initial Pb in lunar rocks. *Earth Planet. Sci. Lett.* **1972**, *14*, 281–304, https://doi.org/10.1016/0012-821x(72)90128-8.
38. Li, X.; Zhou, M.-F. Multiple stages of hydrothermal REE remobilization recorded in fluorapatite in the Paleoproterozoic Yinachang Fe–Cu–(REE) deposit, Southwest China. *Geochim. Cosmochim. Acta* **2015**, *166*, 53–73, https://doi.org/10.1016/j.gca.2015.06.008.
39. Pochon, A.; Poujol, M.; Gloaguen, E.; Branquet, Y.; Cagnard, F.; Gumiaux, C.; Gapais, D. U-Pb LA-ICP-MS dating of apatite in mafic rocks: Evidence for a major magmatic event at the Devonian-Carboniferous boundary in the Armorican Massif (France). *Am. Miner.* **2016**, *101*, 2430–2442, https://doi.org/10.2138/am-2016-5736.
40. Glorie, S.; Jepson, G.; Konopelko, D.; Mirkamalov, R.; Meeuws, F.; Gilbert, S.; Gillespie, J.; Collins, A.; Xiao, W.; Dewaele, S.; et al. Thermochronological and geochemical footprints of post-orogenic fluid alteration recorded in apatite: Implications for mineralisation in the Uzbek Tian Shan. *Gondwana Res.* **2019**, *71*, 1–15, https://doi.org/10.1016/j.gr.2019.01.011.
41. Zeng, L.-P.; Zhao, X.-F.; Li, X.-C.; Hu, H.; McFarlane, C. In situ elemental and isotopic analysis of fluorapatite from the Taocun magnetite-apatite deposit, Eastern China: Constraints on fluid metasomatism. *Am. Miner.* **2016**, *101*, 2468–2483, https://doi.org/10.2138/am-2016-5743.
42. Zhang, X.B.; Guo, F.; Zhang, B.; Zhao, L.; Wu, Y.M.; Wang, G.Q.; Alemayehu, M. Magmatic evolution and post-crystallization hydrothermal activity in the early Cretaceous Pingtan intrusive complex, SE China: Records from apatite geochemistry. *Contrib. Miner. Petrol.* **2020**, *175*, 35, https://doi.org/10.1145/3446999.3447006.
43. Tepper, J.H.; Kuehner, S.M. Complex zoning in apatite from the Idaho Batholith; a record of magma mixing and intracrystalline trace element diffusion. *Am. Miner.* **1999**, *84*, 581–595, https://doi.org/10.2138/am-1999-0412.

44. Palma, G.; Barra, F.; Reich, M.; Valencia, V.; Simon, A.C.; Vervoort, J.; Leisen, M.; Romero, R. Halogens, trace element concentrations, and Sr-Nd isotopes in apatite from iron oxide-apatite (IOA) deposits in the Chilean iron belt: Evidence for magmatic and hydrothermal stages of mineralization. *Geochim. Cosmochim. Acta* **2019**, *246*, 515–540, https://doi.org/10.1016/j.gca.2018.12.019.
45. Harlov, D.E.; Andersson, U.B.; Förster, H.-J.; Nyström, J.O.; Dulski, P.; Broman, C. Apatite–monazite relations in the Kiirunavaara magnetite–apatite ore, northern Sweden. *Chem. Geol.* **2002**, *191*, 47–72, https://doi.org/10.1016/s0009-2541(02)00148-1.
46. Harlov, D.E.; Förster, H.-J. Fluid-induced nucleation of (Y+REE)-phosphate minerals within apatite: Nature and experiment. Part II. Fluorapatite. *Am. Miner.* **2003**, *88*, 1209–1229, https://doi.org/10.2138/am-2003-8-905.
47. Belousova, E.A.; Griffin, W.L.; O'Reilly, S.Y.; Fisher, N.I. Apatite as an indicator mineral for mineral exploration: Trace-element compositions and their relationship to host rock type. *J. Geochem. Explor.* **2002**, *76*, 45–69, https://doi.org/10.1016/s0375-6742(02)00204-2.
48. Migdisov, A.; Williams-Jones, A.; Wagner, T. An experimental study of the solubility and speciation of the Rare Earth Elements (III) in fluoride- and chloride-bearing aqueous solutions at temperatures up to 300 °C. *Geochim. Cosmochim. Acta* **2009**, *73*, 7087–7109, https://doi.org/10.1016/j.gca.2009.08.023.
49. Zhang, W.; Jiang, S.-Y.; Gao, T.; Ouyang, Y.; Zhang, D. Constraints on the Petrogenesis and Metallogenic Setting of Lamprophyres in the World-Class Zhuxi W–Cu Skarn Deposit, South China. *Minerals* **2020**, *10*, 642, https://doi.org/10.3390/min10070642.
50. Li, Z.X.; Li, X.H. Formation of the 1300-km-wide intracontinental orogen and post-orogenic magmatic province in Mesozoic South China: A flat-slab subduction model. *Geology* **2007**, *35*, 179–182.
51. Jingwen, M.; Yanbo, C.; Maohong, C.; Pirajno, F. Major types and time–space distribution of Mesozoic ore deposits in South China and their geodynamic settings. *Miner. Depos.* **2013**, *48*, 267–294, https://doi.org/10.1007/s00126-012-0446-z.
52. Zhou, X.; Sun, T.; Shen, W.; Shu, L.; Niu, A.Y. Petrogenesis of Mesozoic granitoids and volcanic rocks in South China: A response to tectonic evolution. *Episodes* **2006**, *29*, 26–33, https://doi.org/10.18814/epiiugs/2006/v29i1/004.
53. Gaft, M.; Reisfeld, R.; Panczer, G.; Blank, P.; Boulon, G. Laser-induced time-resolved luminescence of minerals. *Spectrochim. Acta Part A Mol. Biomol. Spectrosc.* **1998**, *54*, 2163–2175, https://doi.org/10.1016/s1386-1425(98)00134-6.
54. Marfunin, A.S. *Spectroscopy, Luminescence and Radiation Centers in Minerals*; Springer: Berlin/Heidelberg, Germany, 1979.
55. Morozov, A.M.; Morozova, L.G.; Trefimov, A.K.; Feofilov, P.P. Spectral and luminescent characteristics of fluoroapatite single crystals activated by rare earth ions. *Opt. Spektrosk.* **1970**, *29*, 590–596. (In Russian)
56. Kempe, U.; Götze, J. Cathodoluminescence (CL) behaviour and crystal chemistry of apatite from rare-metal deposits. *Miner. Mag.* **2002**, *66*, 151–172, https://doi.org/10.1180/0026461026610019.
57. Belousova, E.A.; Walters, S.; Griffin, W.L.; O'Reilly, S.Y. Trace element signatures of apatites from granitoids of Mount Isa Inlier, northwest Queensland, Australia. *Aust. J. Earth Sci.* **2001**, *48*, 603–619.
58. Boudreau, A.E.; Kruger, F.J. Variation in the composition of apatite through the Merensky cyclic unit in the western Bushveld Complex. *Econ. Geol.* **1990**, *85*, 737–745, https://doi.org/10.2113/gsecongeo.85.4.737.
59. Perseil, E.-A.; Blanc, P.; Ohnenstetter, D. As-Bearing fluorapatite in manganiferous deposits from St. Marcel—Praborna, Val D'aosta, Italy. *Can. Miner.* **2000**, *38*, 101–117, https://doi.org/10.2113/gscanmin.38.1.101.
60. Seifert, W.; Kampf, H.; Wasternack, J. Compositional variations in apatite, phlogopite and other accessory minerals of the ultramafic Delitzsch complex, Germany: Implications for cooling history of carbonatites. *Lithos* **2000**, *53*, 81–100.
61. Wu, M.Q.; Samon, I.M.; Qiu, K.F.; Zhang, D.H. Multi-stage metasomatic Zr mineralization in the world-class Baerzhe Rare earth element-Nb-Zr-Be deposit. *Am. Mineralogist*. **2022** (in press), https://doi.org/10.2138/am-2022-8336.
62. Qiu, K.F.; Yu, H.C.; Hetherington, C.; Huang, Y.Q.; Yang, T.; Deng, J. Tourmaline composition and boron isotope signature as a tracer of magmatic-hydrothermal processes. *Am. Mineralogist*. **2021**, *106*, 1033-1044.
63. Yu, H.C.; Qiu, K.F.; Chew, D.; Yu, C.; Ding, Z.J.; Zhou, T.; Li, S.; Sun, K.F. Buried Triassic rocks and vertical distribution of ores in the giant Jiaodong gold province (China) revealed by apatite xenocrysts in hydrothermal quartz veins. *Ore Geol. Reviews*. **2022**, *140*, 104612.
64. Jia, F.; Zhang, C.; Liu, H.; Meng, X.; Kong, Z. In situ major and trace element compositions of apatite from the Yangla skarn Cu deposit, southwest China: Implications for petrogenesis and mineralization. *Ore Geol. Rev.* **2020**, *127*, 103360, https://doi.org/10.1016/j.oregeorev.2020.103360.
65. Mercer, C.N.; Watts, K.E.; Gross, J. Apatite trace element geochemistry and cathodoluminescent textures—A comparison between regional magmatism and the Pea Ridge IOAREE and Boss IOCG deposits, southeastern Missouri iron metallogenic province, USA. *Ore Geol. Rev.* **2020**, *116*, 103129, https://doi.org/10.1016/j.oregeorev.2019.103129.
66. Bea, F.; Mitchell, J.N.; Scoates, J.S.; Frost, C.D.; Kolker, A. Residence of REE, Y, Th and U in Granites and Crustal Protoliths; Implications for the Chemistry of Crustal Melts. *J. Petrol.* **1996**, *37*, 521–552, https://doi.org/10.1093/petrology/37.3.521.
67. Gawęda, A.; Sikorska, M. Alkali feldspar megacrysts from the High Tatra granite-indicators of magma mixing/mingling processes. *Mineral. Spec. Pap.* **2009**, *35*, 82.
68. Yu, H.C.; Qiu, K.F.; Hetherington, C.J.; Chew, D.; Huang, Y.Q.; He, D.Y.; Geng, J.Z.; Xian, H.Y. Apatite as an alternative petrochronometer to trace the evolution of magmatic systems containing metamict zircon. *Contrib. Mineral. Petrology*. **2021**, *176*, 68
69. Pan, L.-C.; Hu, R.-Z.; Wang, X.-S.; Bi, X.-W.; Zhu, J.-J.; Li, C. Apatite trace element and halogen compositions as petrogenetic-metallogenic indicators: Examples from four granite plutons in the Sanjiang region, SW China. *Lithos* **2016**, *254–255*, 118–130, https://doi.org/10.1016/j.lithos.2016.03.010.